UNIVERSIDAD DE LAS AMÉRICAS PUEBLA

Engineering School

Department of Industrial, Mechanical and Logistics Engineering

Study on formability and anisotropy effects on Single Point Incremental Forming of Stainless Steel AISI - 304

Thesis that the Student Presents to Complete the Requirements of the Honors Program

Ernesto Jose Quiroz Vazquez

ID 150281

Bachelor's in Mechanical Engineering

Dr. Rafael Carrera Espinoza

Co-Director: Dr. Rogelio Perez Santiago

San Andres Cholula, Puebla. **Autumn 2018**

Signature Sheet

Thesis that the student presents to complete the requirements of the Honors Program **Ernesto Jose Quiroz Vazquez with ID 150281**

Thesis Director

_____

Dr. Rafael Carrera Espinoza

Thesis Co-Director

_____

Dr. Rogelio Perez Santiago

Thesis President

_____

Dr. Jorge Arturo Yescas Hernandez

Thesis Secretary

_____

Dr. Pablo Moreno Garibaldi

Dedicatoria

La realización de este trabajo se debe inicialmente a mi inscripción en el programa de honores, pero esta razón está lejos de ser la más importante. La tentación de abandonar el programa y graduarme por promedio siempre estuvo presente, esta Tesis se la dedico a todas las personas que me impulsaron a terminarla a pesar de las adversidades.

Principalmente le agradezco a mi familia, quienes cada uno, a su manera, me ayudaron a tomar la decisión de enfrentar este gran reto. Especialmente, le agradezco a mi hermana Carmen, a quién después de mencionarle la posibilidad de abandonar el programa, me expresó tajantemente su desaprobación y me recordó que puedo lograr grandes cosas.

Le agradezco totalmente a mi equipo de investigación, al Dr. Rogelio Pérez Santiago por guiarme en el mundo del conformado incremental y darme un empujón necesario cuando todo se veía negro. A Rodrigo Cruz Ojeda, mi compañero y gran amigo, por enseñarme el amor al arte. A Sofía por acompañarme incontables veces en el laboratorio y apoyarme siempre que lo necesitaba.

Le agradezco a mis amigos Gale y Roberto, por darme un parámetro de dedicación y disciplina al cual me pudiera aproximar. Arturo Esquer y Mauricio Vergara, mi banda, por comprender que no podría asistir a los ensayos y que junta a Andrés Govela alegraban mis tiempos de descanso y le dieron un matiz de hermandad a mi paso por la universidad.

Finalmente, le dedico esta Tesis a Mauricio Rodriguez, mi mejor amigo, cuya amistad incondicional prueba superar la distancia y falta de tiempo.

Acknowledgements

The present work could have never been possible without the help from my alma mater, UDLAP, that sponsored great part of my studies and provided me with knowledge and tools to write this thesis. Also, complementing said scholarship, I would like to thank the Roberto Rocca Education Program for providing me with a scholarship to encourage my studies.

Mainly, this thesis could not be possible without the work of my research team. Our mentor, Dr. Rogelio Pérez Santiago, to whom I express my sincere appreciation. My colleagues and friends, Rodrigo Cruz Ojeda, Laura Sofía Fernández Rodríguez, Arturo Javier Belmont Galvez, and Carlos Gerardo Garcia Orduña Caballero.

Furthermore, I would like to thank Dr. Rafael Carrera Espinoza, Dr. Jorge Arturo Yescas Hernández and Dr. Pablo Moreno Garibaldi for the feedback and corrections provided which greatly improved my work. I am especially grateful for the help provided by Dr. Yescas, who as a tutor gave me far more than I expected.

Preface

The present work is the result of many strikes of good, and bad luck, but as I have found out, luck favors those who are persistent. This document is the outcome of hundreds of hours of my own work, and thousands of hours' worth of computational power.

Table of Contents

List of Tables

List of Figures

Abstract

In an ever-changing market with growing demands on the grounds of personalization and rapid prototyping, a process like Single Point Incremental Forming (SPIF) stays relevant for its flexibility and ability to create complex asymmetric shapes without the need of expensive forming dies with the help of an available CNC milling machine.

In the present work, the formability limits of SPIF are explored for sheet metal of stainless steel Stainless Steel AISI - 304 and a thickness of 0.45mm are experimentally measured using Variable Wall Angle quadrangular frusta and finding the maximum forming wall angle.

Also, the effects of anisotropy on wall angle and shell thickness of the frusta (pyramids) on a FEM based simulation are analyzed by means of including true stress-effective strain curve values for 0°, 45° and 90° with respect to the rolling direction of the sheet metal. The results are then compared and evaluated against physical experimental results.

Finally, on the formability analysis an average 79.6° maximum wall angle was found for 0.45mm thick Stainless Steel AISI - 304. Furthermore, the FEM simulation model showed some effects due to the anisotropy of the material, especially on the wall thickness of the parts for 45° with respect to the rolling direction. On the other hand, the simulation proved to need some improvements when compared to the experimental results, especially on the predictability of wall angle. Some recommendations and further work to be done were outlined in the conclusions

Chapter One: Introduction

Single Point Incremental Forming (SPIF), is a type of deformation process, inside the classification of shaping processes, in which sheet metal parts are progressively deformed often with a semispherical tool into a desired shape, while it is being held in place by a blank holder.

Incremental sheet forming is defined by Jeswiet (2005) as a process which has a solid, small-sized tool, instead of large, dedicated dies like in the case of stamping. The forming tool is in continuous contact with sheet metal and moves in 3-dimensional space under control in order to produce asymmetric sheet metal shapes. SPIF is the variant that utilizes a single point for deformation, as opposed to processes that use two points, one on top and one on the bottom of the sheet to support the process.

Figure 1. SPIF tool, blank holder, and lubricated blank

As many researchers have pointed out, the main advantage of SPIF is that there is no need for expensive customized dies as in conventional stamping. SPIF has the capability of producing prototype parts of very complex and asymmetrical shape without the need of a strong initial investment, as long as there is a CNC mill available for use (McAnulty, Jeswiet, & Doolan, 2016).

Nonetheless, the high amount of time it takes to form one part prevents it from directly competing against conventional stamping. Instead, its purpose is to complement it with the possibility of producing small batch sizes and single pieces of highly personalized parts (Perez Santiago, 2012).

A more comprehensive analysis of the classification and characteristics of this process has been recently done by Arturo Belmont (Belmont Galvez, 2018) on a thesis belonging to the same investigation program as the present work. In his thesis, Belmont-Galvez presented how SPIF came to form part of the performable mechanical processes at UDLAP, and also a general comparison with conventional stamping. Please refer to the mentioned work for further information on the topic.

1.1 Thesis Topic and Justification

The main topic of this work is the Single Point variant of Incremental Forming, for short SPIF, done on Stainless Steel AISI - 304 sheet metal of a thickness 0.45mm. The specific aspects of this process researched are two. First, its modeling and simulation by means of Finite Element Method (FEM) simulation with considerations of anisotropy. Second, the Formability by means of defining the maximum wall angle at which a part can be formed.

Research on anisotropy's effects on FEM simulation of SPIF have not been performed on Stainless Steel AISI - 304. Although the formability of this material has already been studied by both Centeno (2014) and Golabi(2014), it has not been done for such a small thickness.

The reason for a sheet metal thickness of relatively small size (0.45 mm) compared to the mainstream of research done, is because of the machine limitations of having a CNC machining mill for educational purposes, in this case an EMCO 500 Concept Mill. There is a strong relationship between the axial force on the tool, and the thickness of the material as presented by (Perez Santiago, 2012). On his work, Perez Santiago uses Aerens' equation for steady state to predict dynamic axial forces and determined them to have good results. Aerens' equation is provided below as equation 1, where Rm is the materials tensile strength, t is the sheet thickness, d is the tools diameter, Δh is the scallop height[11] and α is the forming angle.

1. [1] Scallop height: height of the localized impression of the forming tool on the plane of the sheet being formed (Perez Santiago, 2012)

Therefore, research done on small thickness materials can provide useful information for institutions with small CNC milling equipment to conduct research on SPIF.

$$F_{zs} = 0.0716 R_m t^{1.57} d^{0.41} \Delta h^{0.09} \alpha cos\alpha \quad (1)$$

The material Stainless Steel AISI - 304 was chosen for the sake of results generality, and to contribute to a lack of research on stainless steel incremental forming. Most studies on the topic are focused on Aluminum based materials.

Another advantage of using Stainless Steel AISI - 304 could be its similarity in properties to other materials such as AISI316L stainless steel. This material, due to its anti-corrosive properties, is used in the production of medical implants. Stainless Steel AISI - 304 and AISI - 316L both have similar Tensile Strength as shown in Table 1. Tensile strength is another important indicator of axial force on Aerens' Equation.

From this similarity in some mechanical properties, it is implied that the results from the present work could carry over to 316L stainless steel, which provides grounds for research on the production of medical implants for the skull or the ankle as presented by Ambrogio *et al*. (2005).

Table 1 Properties of Stainless Steels AISI - 304 and AISI - 316L (MatWeb, LCC, 2018)

Property	Density [g/cc]	Ultimate Tensile Strength [MPa]	Yield Tensile Strength [MPa]	Young's Modulus [GPa]
304 SS at 24°C	8	660	295	193
316 L	8	560	290	193

1.2 Objectives

It is the objective of the present work to improve the research capabilities on Incremental Forming in La Universidad de las Americas Puebla by providing useful experimental information that can be applied to the manufacturing of these type of parts.

This is to be achieved by improving and adapting a Finite Element Method simulation model created by Dr. Rogelio Perez Santiago and by setting a precedent in material characterization for the Single Point Incremental Forming (SPIF) process with the tools and machinery available at UDLAP.

Furthermore, it is an objective of this work to find a formability indicator for Stainless Steel metal sheets during the SPIF process that can aid in future design decisions of more complex parts.

Therefore, the following research questions are posed to direct this work:

1. Is there a significant anisotropic behavior on the Stainless Steel AISI - 304 sheets currently used for SPIF forming of parts? And if so, what is its effect on the geometry formed and effective plastic strain on the part?
2. Is the current Finite Element Method simulation model being used suitable for predicting the geometry of manufactured parts?
3. What is the maximum forming angle possible for the 0.45 mm thick Stainless Steel AISI - 304 material with the current tools and machinery at UDLAP?

Chapter Two: Literature Review

2.1 Formability in Single Point Incremental Forming (SPIF) Literature Review

Formability as the name implies, is the ability of a material, in this case sheet metal, to be molded to a desired shape without presenting cracks. Formability is closely related to the elongation of the material which is the total amount of strain during a process.

Formability in Single Point Incremental Forming (SPIF), commonly named *Spifability* has been a topic of discussion for several years. Measuring formability for SPIF processes has been performed in many ways. Traditionally a forming limit diagram has been used for this purpose. Alternative methods are for example, the one used by Hussein and Gao (2007) where they utilized the thinning limits of sheet metals to obtain a quantitative value for the formability.

In the present work, maximum wall angle has been chosen to describe formability for its practicality and effectiveness. This method has been used by many researchers including Hussain, Gao and Ziran (2008), Jeswiet and Micari (Asymmetric Single Point Incremental Forming of Sheet Metal., 2005). “In SPIF, the maximum forming angle before the occurrence of fracture is considered as a formability measure of the sheet metal.” (Shamsari, Mirnia, Elyasi, & Baseri, 2017)

The maximum wall angle is described as the angle between the plane perpendicular to the axis of the tool used, and the wall being formed. Represented as θ, it can be visualized in Figure 2.

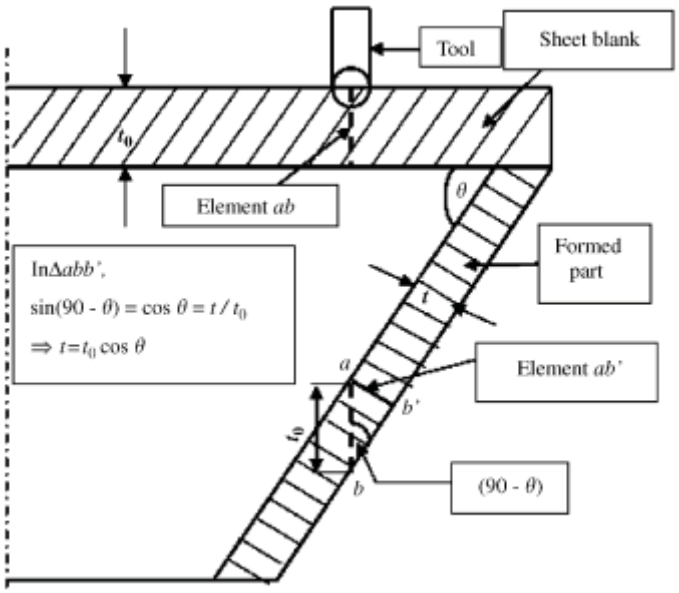

Figure 2. Schematic illustration of the Cosine's law (Hussain & Gao, 2007) .

Also, in Figure 2 the Cosine's law is showcased, Wei *et al*. (2004) have showed by performing several experiments that the thickness distribution in a negative incremental formed part follow the cosine law, which declares that given an initial thickness t_0 and the forming slope angle θ, the final thickness at said slope is given by the following equation.

$$t = t_0 cos\theta$$

With this considered, it can be deduced that a 90° wall angle cannot be formed since the final thickness would be zero.

The influence of several forming parameters on the formability has been summarized by McAnulty Jeswiet and Doolan on their article: "*Formability in single point incremental forming: A comparative analysis of the state of the art* (2016)."

In this article the influence of parameters such as sheet thickness, tool diameter and shape, feed rate, spindle speed, and step down found by a myriad of researchers was cited and displayed. Inside this description the material used through each paper was also noted. Since the material used for the present work is Stainless Steel AISI - 304, special attention was put on the information for this particular material.

The increase of material thickness was found to have a positive effect on formability on the research conducted by Golabi. (Golabi & Khazaali, 2014). In this study, a material thicknesses used were 0.5 and 0.7 mm. In comparison, the sheet metal thickness used for the present work was 0.45 mm thick. According to Golabi, this would hinder formability.

Tool diameter has a similar effect, its increase in turn yields an increase in formability as reported by Golabi (2014). On the other hand, Centeno (2014) reported the opposite relationship between tool diameter and formability. The tool diameters used by Centeno were 6, 10 and 20 mm, while the ones used by Golabi were 6 and 14 mm in diameter. Therefore, the results are non-conclusive, and instead of being a direct or indirect relationship, tool diameter must be optimized for a particular set of experiment parameters.

Step down is defined as the movement in the tool's axial direction after every turn in incremental forming. As reported by McAnulty *et al*. (2016) most papers, 13 out of 18, determined that a decrease in step down meant an improvement in formability. On this parameter, Golabi (2014) and Centeno (2014) did agree on decreasing the stepdown to improve formability.

The effects of feed rate were found to be non-significant by Golabi (2014). In this paper 600 and 1200 rpm were used. Papers evaluating the effect of feed rate on Titanium, AA3003-0, AA2024-T4 and polypropylene, found that a decrease on this parameter improved formability (McAnulty, Jeswiet, & Doolan, 2016).

Finally, until 2016 the effects of spindle speed on Stainless Steel AISI - 304 formability have not been studied. Nonetheless, most papers for other materials suggest increasing the spindle speed to increase formability. On the other hand, high spindle speeds increment tool wear, and demand a higher use of lubricant which has economic and environmental repercussions.

2.2 Anisotropy in Single Point Incremental Forming (SPIF) Literature Review

Anisotropy is defined as the property of a material to exhibit variations in its physical, or in this case, mechanical properties along different axes. This is due to the crystallographic structure and the nature of the rolling process with which sheet metal is manufactured. Anisotropy is quantified by the Lankford parameter, which is a ratio of the strains in width and thickness directions during a uniaxial tensile test.

During the review of literature for the preparation of this thesis, an important lack of information about the effects of anisotropy on the SPIF process was found. In an article focused of determining the frustum depth of Stainless Steel AISI - 304 stainless steel plates using incremental forming, the authors briefly mention the effects of anisotropy as non-

influential on the process (Golabi & Khazaali, 2014). They do so by citing the work done by Fratini *et al*. in 2004 on the influence of mechanical properties on SPIF formability.

Upon further reading of the cited article, the materials used were High Strength Steel, Deep Drawing Quality steel, AA1050-0, AA6114 T4, Brass and Copper (Fratini, Ambrogio, Di Lorenzo, Filice, & Micari, 2004). There is no mention of Stainless Steel in this article.

A summary of the findings by Fratini et al. can be visualized in Table 2. In this table, various material properties are classified on their influence on the maximum strain while the minimum strain is 0 (FLDo) of both conventional forming processes and incremental forming processes. In this table, K is the strength coefficient, n is the strain hardening coefficient and Rn is the normal anisotropy index.

Table 2 Influence of the input variables and their Interactions on FLDo and FLDoincre (Fratini, Ambrogio, Di Lorenzo, Filice, & Micari, 2004).

Predictor	Influence on FLD_0	Influence on FLD_{0incre}
K	High	Medium
N	No	High
Rn	High	Low
UTS	No	No
A%	No	Medium
K*n	High	High
K*Rn	No	No
n*UTS	High	No
n*A%	No	Medium

This Article by Fratini *et al.* was also disputed by Hussain *et al.* on the grounds that few materials were tested and they all had relatively big hardening exponents, therefore their conclusions could not be generalized. Hussain *et al.* found that neither K or n are the more influential parameters on formability, they conclude that the percent tensile reduction of area is the sole major material property influencing spifability. (Hussain G. , Gao, Hayat, & Ziran, 2008).

Another mention of the effects of anisotropy was found on a more recent study on the forming behavior of AA-6061 aluminum during SPIF (Kumar Barnwal, Chakrabarty, Tewari, Narasimhan, & Mishra, 2018). In this article, aluminum sheets were formed into conical shapes, and the major and minor strains were measured by means of a Digital Image Correlation method. Also, Finite Element Method simulations were performed to compare the results. Finally, a detailed microstructural study was carried out, using specimens from deformed parts of the cone, and intact parts of the cone.

The FEM simulations were done on PAMSTAMP 2G, a commercial software oriented to the simulation of sheet metal forming. It was performed with a mesh size of 1mm with four node elements for the blank of sheet metal. The material properties in the FEM model included a plastic anisotropy factor "r" for the Rolling Direction (RD), 45° to Rolling Direction (ID), and 90° to rolling direction (TD). These properties are included in Table 3.

The conclusions reached by Kumar *et al*. are as follows. First, the major strain during Single Point incremental forming is always perpendicular to the direction of the tool movement. Second, FEM results are in accordance to the experimental data but, more

accurate results can be achieved by using a finer mesh size. Third, for this aluminum, the highest resistance to deformation was found in the ID direction, 45° from rolling direction, attributed to a higher Taylor factor with respect to RD and TD orientations.

Table 3 Mechanical properties of AA-6061 (T6) aluminum alloy obtained using tensile tests and r-bar tests (Kumar Barnwal, Chakrabarty, Tewari, Narasimhan, & Mishra, 2018).

	PS (MPa)	UTS (MPa)	Elongation (%)	K	n	Plastic anisotropy	$\bar{r}_{mean}$
RD	265	308	14.45	416	0.10	$r_0 = 0.558$	0.70
ID	255	293	12.36	415	0.10	$r_{45} = 0.70$	
TD	238	274	13.06	406	0.09	$r_{90} = 0.833$	

PS proof stress, *UTS* ultimate tensile strength, K strength coefficient, n strain hardening exponent

In Figure 3 a notable difference between the experimental and simulation strain results can be observed, in the cited work, it is attributed to a coarse mesh size due to computational limitations.

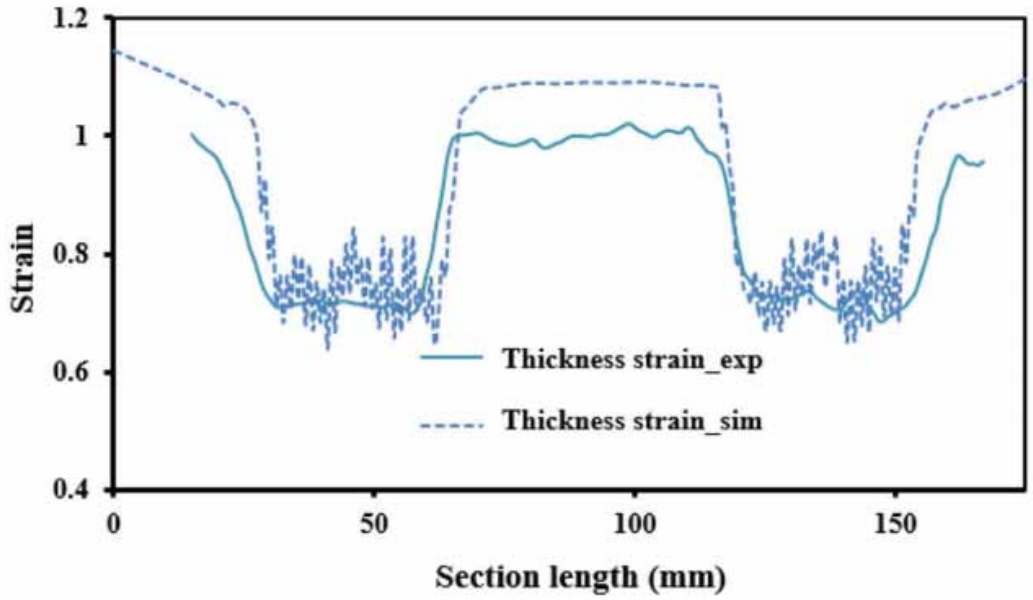

Figure 3. Experimental and Simulation thickness strain results (Kumar Barnwal, Chakrabarty, Tewari, Narasimhan, & Mishra, 2018).

From the review of the state of the art on anisotropy it can be concluded that further research should be conducted. The available information on anisotropy's effects on formability are generally performed on aluminum samples. Specific analysis of the effects of anisotropy of Stainless Steel AISI - 304 was not found.

Chapter Three: Methodology

3.1 Characterization Methodology

The material used in the present work is Stainless Steel AISI - 304. Its general properties were obtained from the available datasheet online (MatWeb, LCC, 2018) which coincides with the material properties used by other researchers such as Golabi and Khazaali (2014). These properties are 8 g/cm^3 for density, 193 GPa for Young's modulus and 0.29 for Poisson's ratio.

To define the material's behavior under plastic strain, True Stress vs Effective Plastic Strain curves were obtained from tensile tests for 0, 45, and 90 degrees with respect to the rolling direction of the Stainless Steel AISI - 304 sheet metal.

The initial Force vs Deformation curves were obtained by means of tensile tests performed in the WDW-300E Universal Testing Machine in accordance to the ASTME8 Standard Test Methods for Tension Testing of Metallic Materials

Figure 4. Tensile Test being performed with Epsilon Extensometer.

Eight test specimens were manufactured using a laser cut machine with the dimensions established by the ASTM E8 standard, Table 4 shows specimen number and the orientation with respect to the rolling direction.

During the tensile tests, extensometers provide an average of the deformation inside of the testing area. This information is reliable at low deformations, but closer to the fracture point, necking and stress concentrations start to occur. Therefore, to try and characterize the Stainless Steel AISI - 304 better, attempts at measuring deformation with image correlation technology were made.

This consisted of applying speckles on the specimen with paint and taking picture every 2 seconds. The images would then be processed by the GOM Correlate Software and would give a whole spectrum of deformations inside the testing area, instead of just an average. The advantages of these method have been well documented in the article, *Whole Field Sheet-Metal Tensile Test Using Digital Image Correlation* (Wang, et al., 2010).

Table 4 Specimen ID with corresponding orientation

Specimen ID	1	2	3	4	5	6	7	8
Orientation	0°	0°	0°	45°	45°	45°	90°	90°

The Tensile tests with image correlation were not successful, and they are considered as valuable future work to better characterize the materials for Single Point Incremental Forming.

Nonetheless, four successful tensile tests were carried out, with test specimens 2, 4, 5 and 8, with 0°, 45°, 45°, and 90° in orientation respectively.

The force-deformation curves delivered by the test were corrected and converted first into Engineering Stress vs Engineering Strain, then into True Stress vs True Strain and finally into True Stress vs True Plastic Strain (referenced as Hardening curves in the rest of this document) which accounts for the reduction of area in the specimen during the tensile test. Figure 5, Figure 6, and Figure 7 show this process.

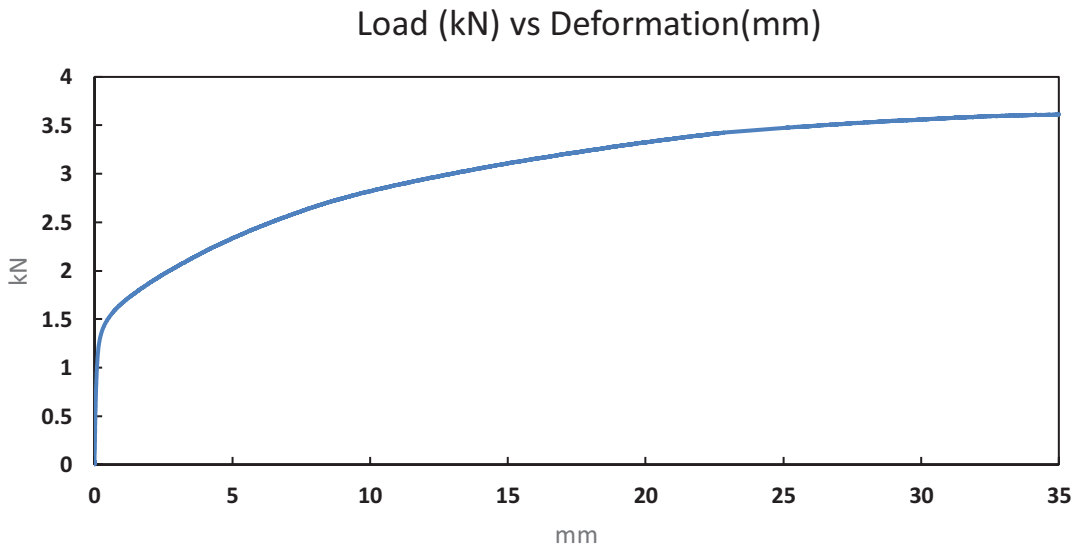

Figure 5. Load vs Deformation Curve

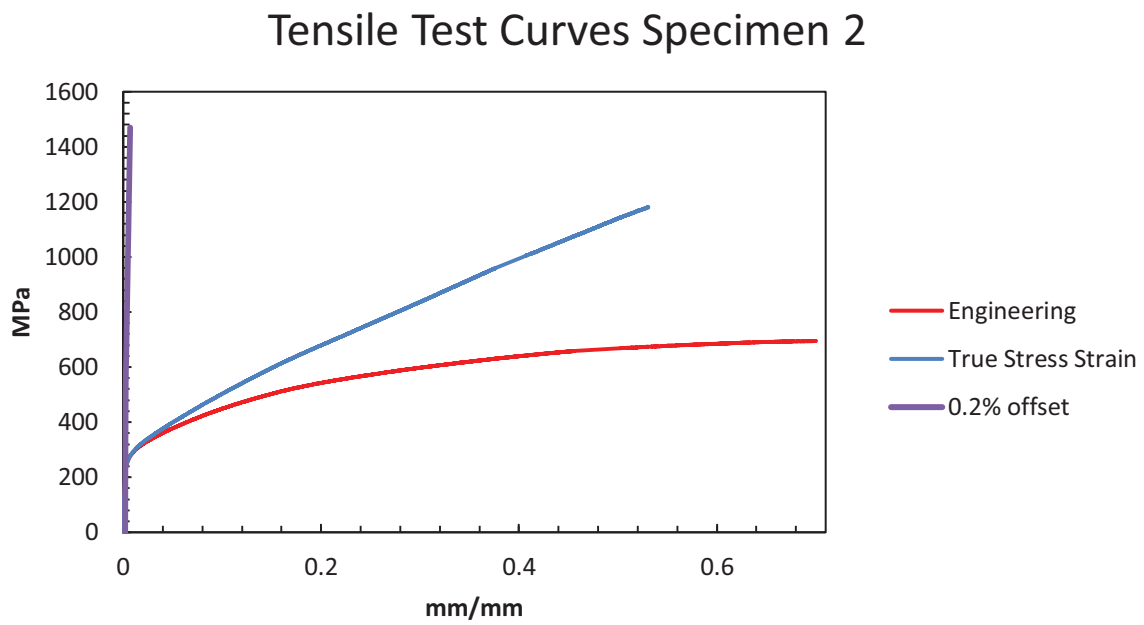

Figure 6. Engineering Stress vs Engineering Strain (red) and True Stress vs True Strain (blue)

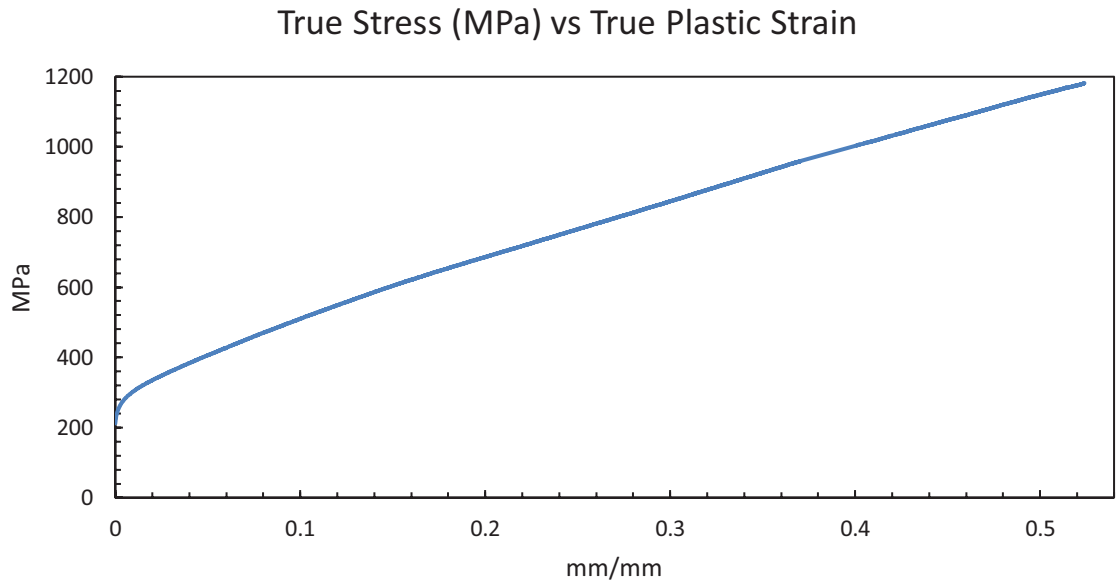

Figure 7. True Stress vs Effective Plastic Strain

The resulting curves were then compared with the ones done by Perez Santiago (2012) and similar values were found.

The data obtained from the True Stress vs True Plastic Strain curve would be then used in the Finite Element Analysis simulations to model the plastic behavior of the Stainless Steel AISI - 304 sheet used in the present work.

3.2 Experimental Methodology

The experiments carried throughout this work can be classified in two, according to the general shape manufactured. They are Uniform Wall Angle (UWA) experiments, and Variable Wall Angle (VWA) experiments. Both share a general experimental methodology but differ in key elements such as their purpose.

UWA parts were formed to verify the accuracy of the Finite Element Analysis model used in the present work by providing physical results to which compare the simulation results.

The objective of the VWA parts formed, is to obtain a measure for formability by finding the maximum wall angle at which this process can be carried out.

The current chapter contains both a general and specific methodologies for the undergone experiments.

3.2.1 General SPIF Methodology

Several parts were formed during the course of the present work, and a general experimental methodology was used for all of them.

First, the desired geometrical, or product, parameters were defined, this include the initial sheet thickness, the general shape (cone, pyramid), type of wall (variable wall angle or uniform wall angle), width of the pyramid at the top (diameter in the case of a cone), the initial forming angle, the stepdown (tool pitch), the amount of steps which define the height of the part, and generatrix radius (zero for uniform wall angle parts).

Then, the process parameters are defined. These are tool radius, spindle speed, feed rate and lubrication rate. These parameters along with the geometrical parameters can be seen in Table 5. In Figure 8 some of these parameters are also depicted.

Table 5 List of Parameters used in SPIF with typical values

Parameters	**Symbol/Representation**	**Typical values for the present work**
Sheet Thickness	t_0	0.45466 mm
General Shape	N/A	Pyramid
Wall type	N/A	VWA and UWA
Width	w	70 mm
Initial Forming Angle	β	45° and 55°
Step Down	Δz	0.25 mm
Number of Steps	Nz	80
Generatrix Radius	R	35° and 50°
Tool Radius	r_t	3.175mm
Spindle Speed	S	1250 rpm
Feed Rate	f	500 mm/min
Lubrication Rate	l	Once every 5 mm of height

All these parameters are then inserted into a python subroutine named zir106.py detailed in appendix C, which writes a .mpf file with the G-code necessary to shape the desired part using an EMCO Concept Mill 55® CNC machine.

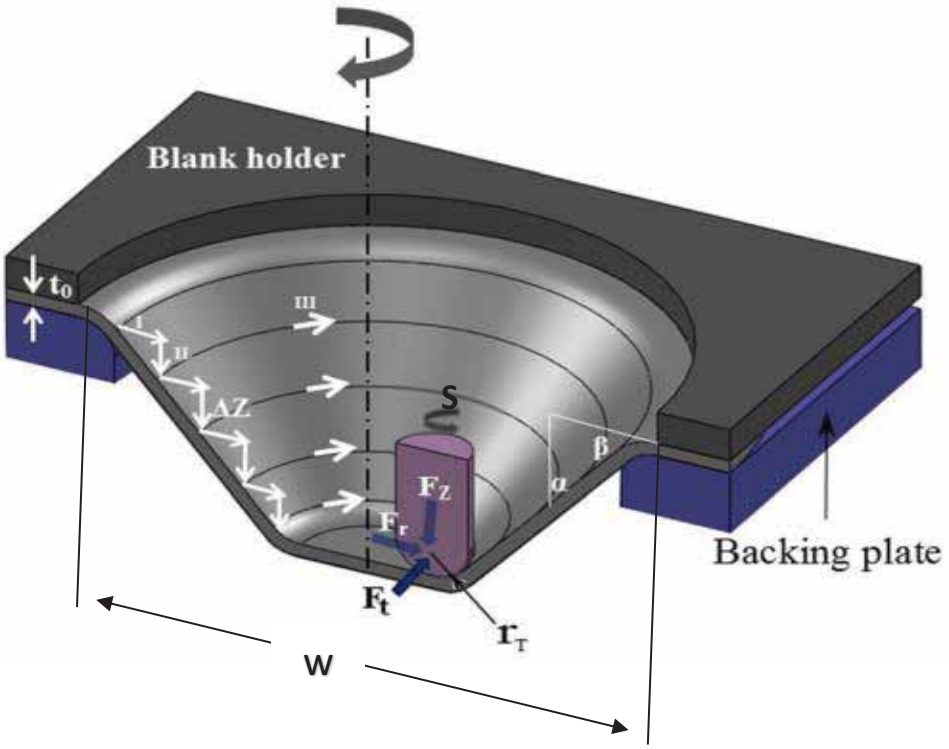

Figure 8. Visualization of some general parameters (Hussain G. , Gao, Hayat, & Ziran, 2008)

Next, the machine and its components are prepared for the forming process. The sheet metal is secured into the blank holder and subsequently the blank holder is secured to the CNC mill. The appropriate tool is selected, and the work offset is defined by setting the origin at the middle of the sheet, with the tool touching the surface lightly. Finally, lard (pig fat oil) was applied to the sheet as lubricant.

Before starting the forming process, the tool is elevated, and the work feed dial is set down to 20%, this in order to supervise the beginning of the process in which any important mistake in the parameters can be observed and corrected before damaging the machine.

Figure 10. Blank Holder with lubricant.

Figure 9. CNC Milling machine EMCO concept MILL 55 taken from *(Belmont Galvez, 2018)*

The equipment used can be seen in Figure 9 and Figure 10. In the program section of the control panel, the G-code is reviewed and executed. During the forming process there should be a pause every 5 mm in the Z direction to remove the used lubricant and apply unused lubricant again. The pause is executed by adding an M0 command on the g-code after every 5mm in the Z direction. Using the pause button on the machine keyboard will interrupt the process and go to the beginning of the code again, this should be avoided.

Finally, when the process is done, the lubricant is removed, and the blank holder unfastened. The final part is cleaned and analyzed depending of the intention of the experiment.

3.2.2 Uniform Wall Angle (UWA) Parts Forming and Analysis Methodology

Three UWA pyramidal parts were formed with the parameters listed in Table 6. After being formed they were 3D scanned using ATOS Core by GOM hardware with the program GOM Scan 2016 in order to obtain a cloud of points. This information was then analyzed using GOM inspect 2018 software to retrieve thickness data along the cross section of the parts. Also, an average plane was created virtually on each wall to compare it to the horizontal plane and therefore obtain the wall angle. An illustration of the scanned parts can be seen in Figure 11 and in Figure 12. These results were the compared to the thickness and wall angle values obtained from FEM simulation.

Table 6 Parameters of formed UWA parts.

Width [mm]	Forming Angle [°]	Step Down [mm]	Number of Steps	Tool Radius [mm]	Spindle Speed [rpm]	Feed Rate [mm/min]	Lubrication Rate
67.4	45	0.25	80	3.175	1250	500	Every 5 mm

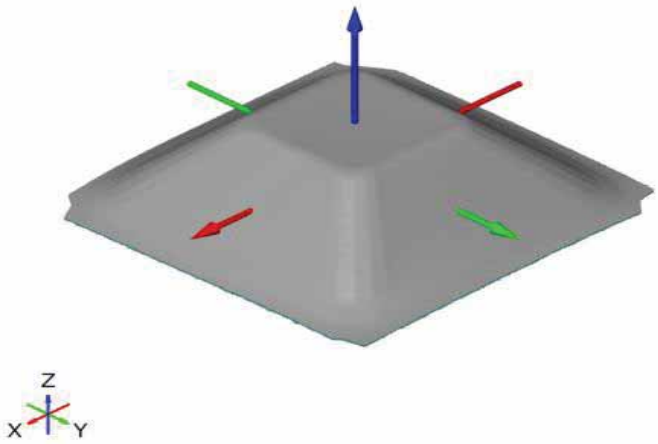

Figure 11. Scanned image of pyramid 20

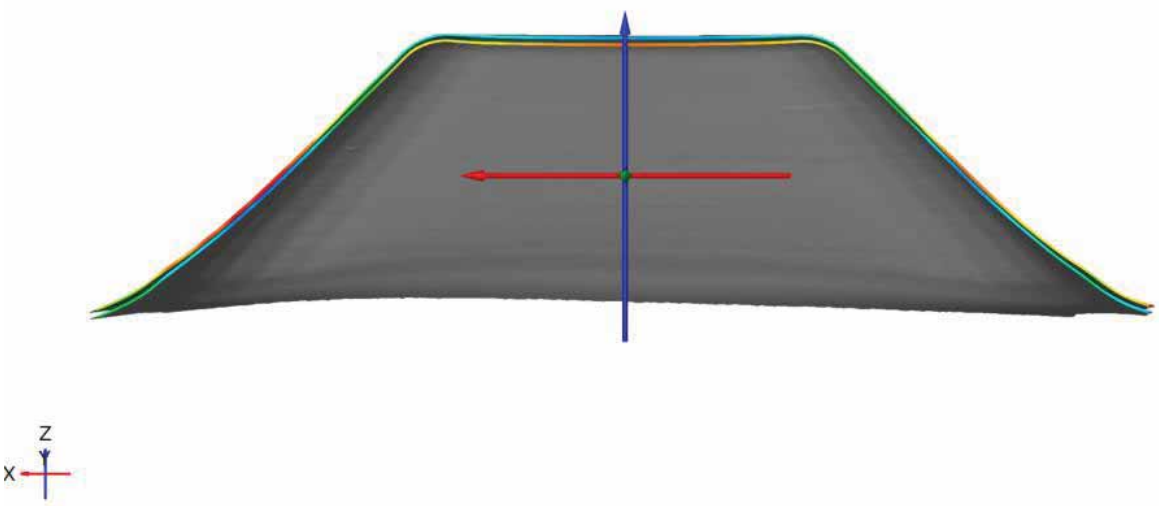

Figure 12. Virtual Cross Section of Pyramid 20.

3.2.3 Variable Wall Angle (VWA) Parts Forming and Analysis Methodology

The purpose of forming VWA parts in the present work, is to find an indicator of the formability of the Single Point Incremental Forming with our research parameters.

The research of Hussain and Gao (2008) showed that using a variable wall angle geometry, the amount of experiments necessary to determine the formability, also called *spifability*, of a sheet metal are greatly reduced.

Therefore, two different sets of three experiments each were designed to find a parameter that can define the formability of our material, Stainless Steel AISI -304, under our main conditions of work. The experiment parameters can be seen in Table 7. The sheet metal used was 0.45 mm thick.

Table 7 Experiment Parameters for Sets A and B.

Experiment Set	Pyramid Width [mm]	Initial Wall Angle	Step Down [mm]	Tool Radius [mm]	Lubricant	Spindle Speed [rpm]	Work Feed [mm/min]	Generatrix Radius "R" [mm]
A)	70	55°	0.25	3.175	Lard	1250	500	35
B)	70	55°	0.25	3.175	Lard	1250	500	50

Trajectories were defined to follow a variable wall angle geometry which would start with a 55° angle and finish at 90°. Fracture is expected to occur at a θ value between 60 and 90 degrees. It is impossible for a part to be formed by means of negative incremental sheet forming at 90° because the thickness of the wall would become zero according to the Cosine Law of thickness distribution (Hussain & Gao, 2007). A visualization of the geometrical parameters can be appreciated in Figure 13.

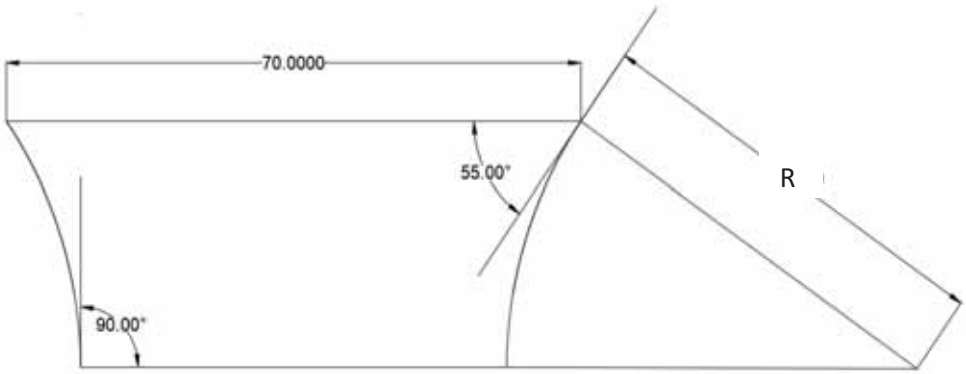

Figure 13. Geometrical Parameters

As it was described in the review of literature, according to McAnulty *et al*. (2014) *spifability* changes with the alteration of most of the parameters in a way that is not always predictable. To obtain results that are significant to our work, we maintained the work feed, spindle speed,

lubricant, tool radius and step down in accordance to the rest of the experiments performed throughout this work.

Nonetheless, in order to make the results more robust and improve their reliability, the generatrix radius was changed from 35mm to 50mm in set one and two of experiments, respectively. Both trajectories can be visualized in Figure 14 and in Figure 15.

The experiments were carried out by using a Python subroutine to obtain a G-Code to be entered on the EMCO 500 Concept CNC Machining Mill. For further information regarding the VWA pyramid forming process, refer to the General Experimental Methodology on Chapter 5.

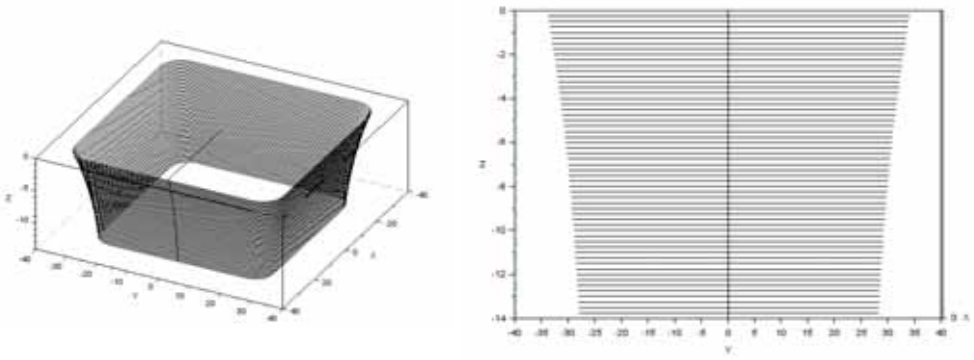

Figure 14. Trajectory of experiment set A with 35mm generatrix radius, isometric and front view.

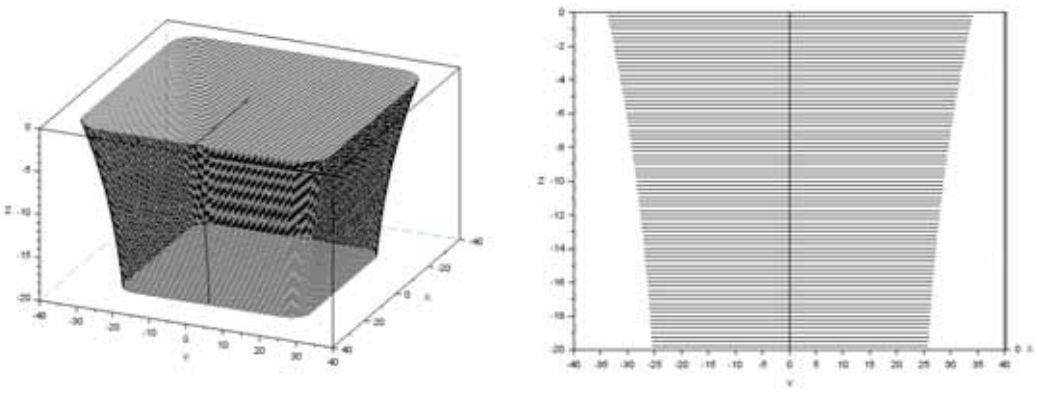

Figure 15. Trajectory of experiment set B with a 50mm generatrix radius, isometric and front view.

With the purpose of finding the angle at which fracture occurs, the position along the z axis of the trajectory, or depth of the pyramid, at the moment of fracture is registered. This position can be then assigned to a corresponding θ value according to the geometrical relationship in equation 2. where θ_p is the forming angle at point p, y_p is the distance in the y direction from the center of the generatrix circle to point p, and R is the generatrix radius. This relationship is further explained on the review of the literature of formability (Hussain & Gao, 2007)

$$\theta_p = cos^{-1}\left(\frac{y_p}{R}\right) \qquad (2)$$

Also, the depth at fracture for each pyramid was later used to find the maximum plastic strain at the moment of fracture in the FEM simulations.

3.3 Finite Element Analysis Methodology

The FEM model was created by Perez-Santiago for his Ph.D. dissertation in 2012. This model and methodology has been modified and improved to fit the context research at Universidad de las Americas Puebla.

3.3.1 Finite Element Analysis Methodology in General

In this thesis, the finite element analysis (FEA) was used to simulate the Single Point Incremental Forming Process with the specifications particular to the equipment available in La Universidad de Las Americas Puebla, although it can be adapted to processes done elsewhere.

This general FEA Methodology applies for the subsequent chapters on Simulation Methodology.

3.3.1.1 Parts definition

The steps taken to perform simulations using FEA started with the computer assisted drawing of our setup using the software CREO Parametric 4.0®. These drawings included the tool with its clamping device, the blank holder and the blank. Each of these components would become the three parts involved in the FEA.

3.3.1.2 Meshing

Afterwards, the resulting CAD files were uploaded to LS Pre-Post software to simplify and discretize the geometry into finite elements. The blank that was to be deformed was meshed with square elements of 0.75mm per side. A relatively small sized mesh is necessary for the blank since it is the part to be deformed. The tool was meshed with elements of 0.6 mm per side near the tip of the tool. The meshing of the blank holder is not important, since it was only used to define a movement constraint where it contacts the blank. All the elements in the model were defined as default shell elements.

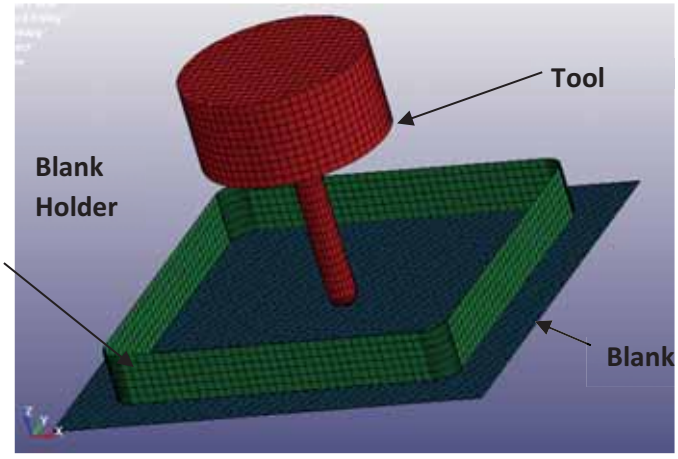

Figure 16. Meshed tool, blank and blank holder.

3.3.1.3 Material Designation

Diferent materials were defined for the blank and the tool. For the tool a rigid material with general steel properties was used as it is shown in Table 8. These properties are 7.85 g/cm^3 for density, 207GPA for Young's Modulus and 0.3 for Poisonn's ratio.

Table 8 Properties for tool material.

TITLE							
rigid punch							
MID	RO	E	PR	N	COUPLE	M	ALIAS
1	7.850e-06	207.00000	0.3000000	0.0	0	0.0	

The material used for the blank was Stainless Steel AISI - 304 with the properties taken from matweb.com (MatWeb, LCC, 2018) which coincide with the properties used by Golabi and Khazaali in their research on incremental forming of Stainless Steel AISI - 304 (Golabi & Khazaali, 2014). The properties used are 8 g/cm^3 for density, 193 GPa for Young's modulus and 0.29 for Poisson's ratio.

Table 9 Properties for blank material entered into LS-PrePost

TITLE							
AISI-304 material model example (kg-mm-ms-kN-GPa)							
MID	RO	E	PR	SIGY	ETAN	FAIL	TDEL
1	8.000e-06	193.00000	0.2900000	0.2122000	0.0	1.000e+21	0.0

For the simulations, four different materials were used for the blank. All of them Stainless Steel AISI - 304 but with different directions compared to the rolling orientation, 0°, 45°, 90° and an isotropic material without a particular direction. The material's behavior under plastic

deformation was inserted into the simulation by adding the values of the strain hardening curve obtained with tensile tests for all three directions.

3.3.1.4 Boundary Conditions

The blank was constrained in the nodes that were in contact or outside the blank holder to simulate the function of the real blank holder. The constraint was fixed in all three directions and rotations.

The contact between the blank and the tool was defined as “contact forming one way surface to surface” which defines a master surface (tool) and a slave surface (blank).

3.3.1.5 Prescribed Motion.

The motion of the tool is given by velocity curves that define the movement in x, y and z directions of the tool. These curves are obtained by runing the second python subroutine called velzir5b.py ,which is included in appendix C, after obtaining the coordinate file “pathxyz.dat” by running the first python subroutine “zir106.py” ,also included in appendix C, with the desired parameters as described in Chapter 3.2.1.

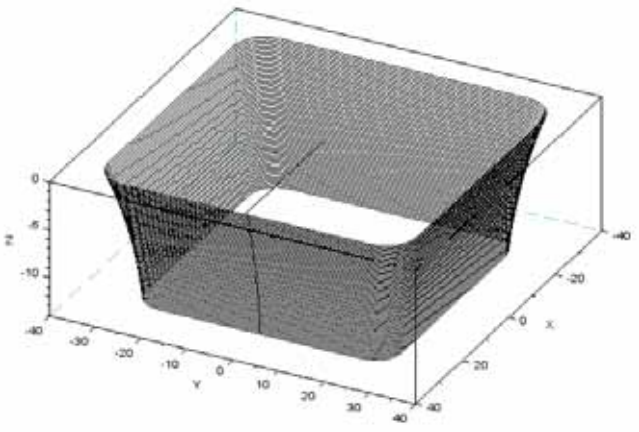

Figure 17. Trajectory defined by file "pathxyz.dat" for a VWA part

The model is then solved using LS-Dyna processor, and the results visualized and analyzed using LS-PrePost.

After this general methodology, further steps were taken in particular for the analysis of either UWA parts or VWA parts depending on the objectives of the experiment. These steps are detailed in the following sections.

3.3.2 Uniform Wall Angle (UWA) Finite Element Analysis Methodology

While the FEA simulation gives a myriad of results including stress, force displacement and strain; the purpose of the simulation for UWA parts for this study is to obtain the distribution of thickness and the wall angles against the horizontal plane. These results are then to be compared to the experimental results from the formed pyramids using the EMCO 500 Concept CNC mill.

3.3.2.1 Thickness distribution

To obtain the thickness distribution with LS-PrePost, a section along plane XZ and a section along plane YZ are cut while the shell thickness results are being displayed.

a)

b)

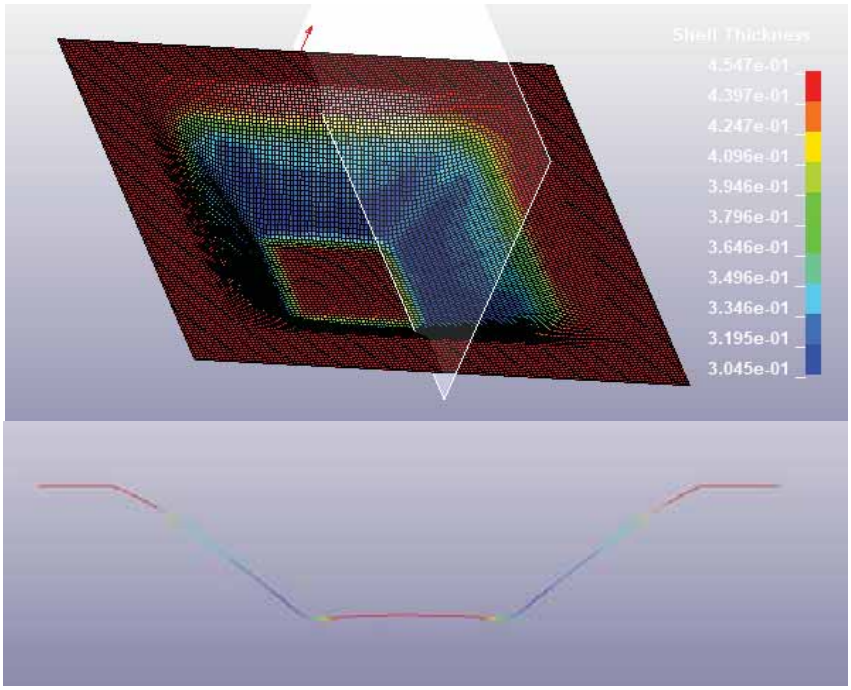

Figure 18. a) YZ plane on thickness results b) corresponding cross section.

The results along the cross section can then be plotted, but the abscissas value will correspond to the distance along the cross section instead of the absolute position along X or Y axis. This plot can be cross referenced with a plot of the Y or X coordinate along the cross section to obtain a plot of Thickness vs X (or Y) coordinate. These plots can be seen in Figure 19, Figure 20, and Figure 21.

The resultant plot is then downloaded as a .csv document to be analyzed even further.

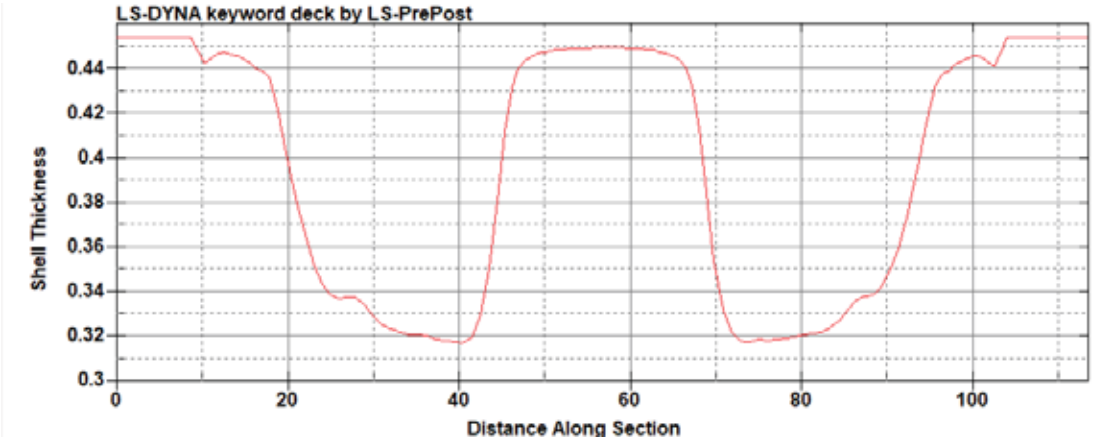

Figure 19. Thickness along section

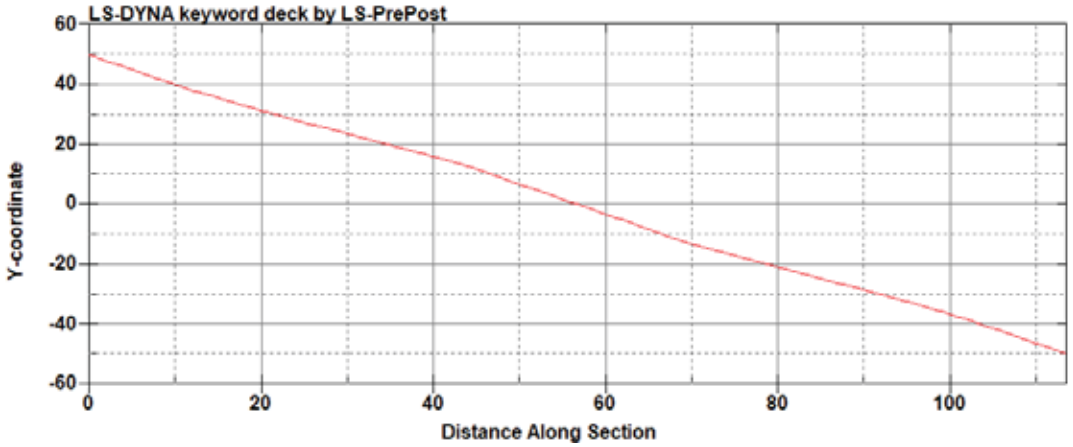

Figure 20. Y coordinate along section.

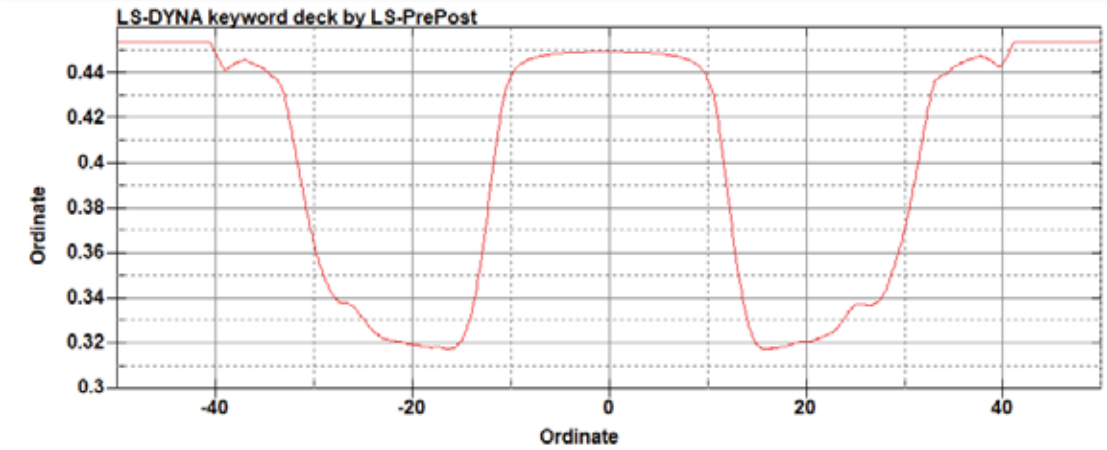

Figure 21. Cross referenced plot. Thickness vs Y coordinate

3.3.2.2 Wall Angle Measurement

The wall angle is a very characteristic geometrical property of a formed Uniform Wall Angle part. This angle θ is the acute angle described between the horizontal plane, and the plane of any of the four walls of a pyramidal part. A simple depiction of this angle can be seen in Figure 22.

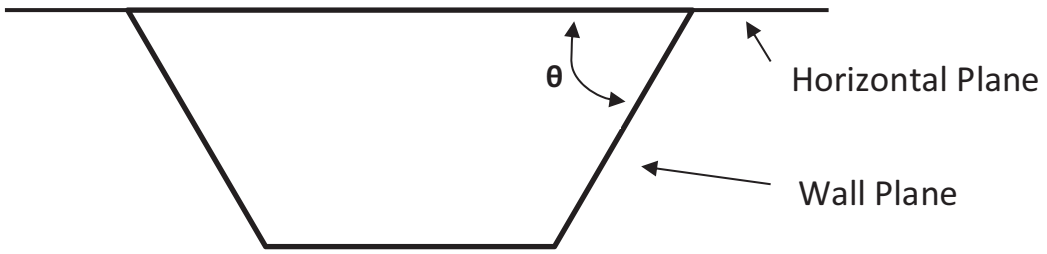

Figure 22. Simple illustration of the Wall Angle

This parameter can be used to measure the geometrical precision of both the physical forming process and the simulated one.

Therefore, the software LS-PrePost was used to measure the resulting wall angles of the various simulations to later compare them against the angles achieved with the actual SPIF processes that were carried out.

After obtaining the results for the FEM analysis, two planes were created, one for the wall, and one for the horizontal plane. The wall plane was achieved by using a fitting plane operation in the software, taking as many elements from the wall as possible. The same operation was used on the elements that were not deformed at the edges of the blank in order to obtain the horizontal plane. Fig 25 shows these planes on top of the FEM model.

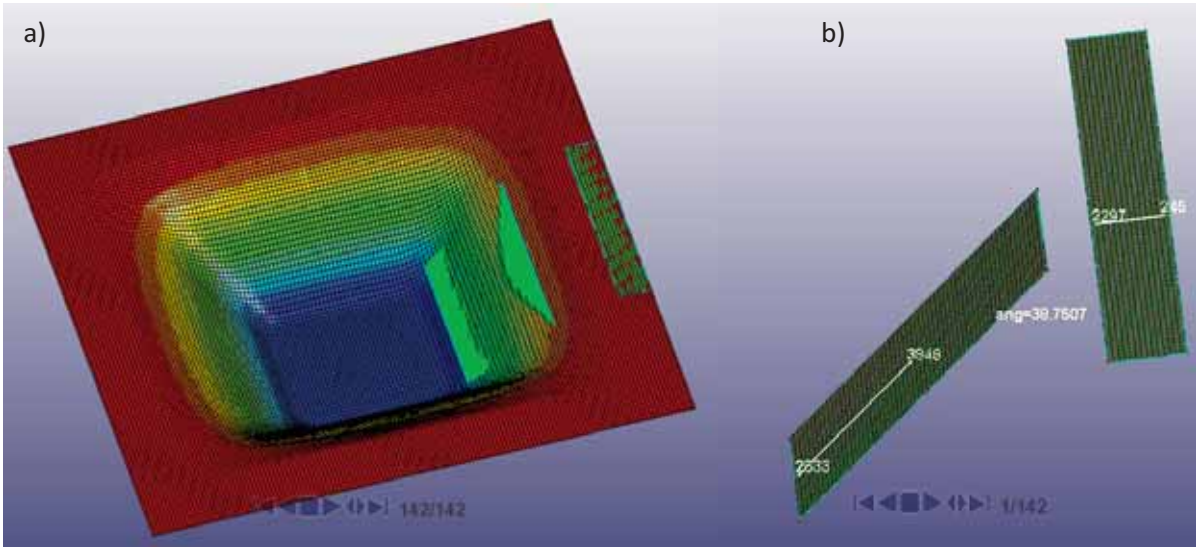

Figure 23. Fitted Wall and Horizontal Planes a) with corresponding part and b) without corresponding part.

Finally, the angle between the two planes is measured and registered to be compared.

3.3.3 Variable Wall Angle (VWA) Finite Element Analysis Methodology

For the present work, the VWA parts were formed with the purpose of establishing a formability limit based on the maximum wall angle that can be formed. This was done experimentally. The simulation was carried out to get an estimated maximum effective plastic strain at which the fracture occurs at said maximum angle.

The VWA simulations were designed to finish until the tool is at a 90° forming angle with the blank. This is the theoretical limit according to the sine law of thickness distribution discussed in the review of literature. Fracture always happens before the 90 degrees, and z position of the tool for each fracture during the experiments is known.

Therefore, it is necessary to look at the results at the time of fracture, and not at the end of the simulation. Once the results for the corresponding z displacement are being shown, the maximum effective strain is noted.

a)

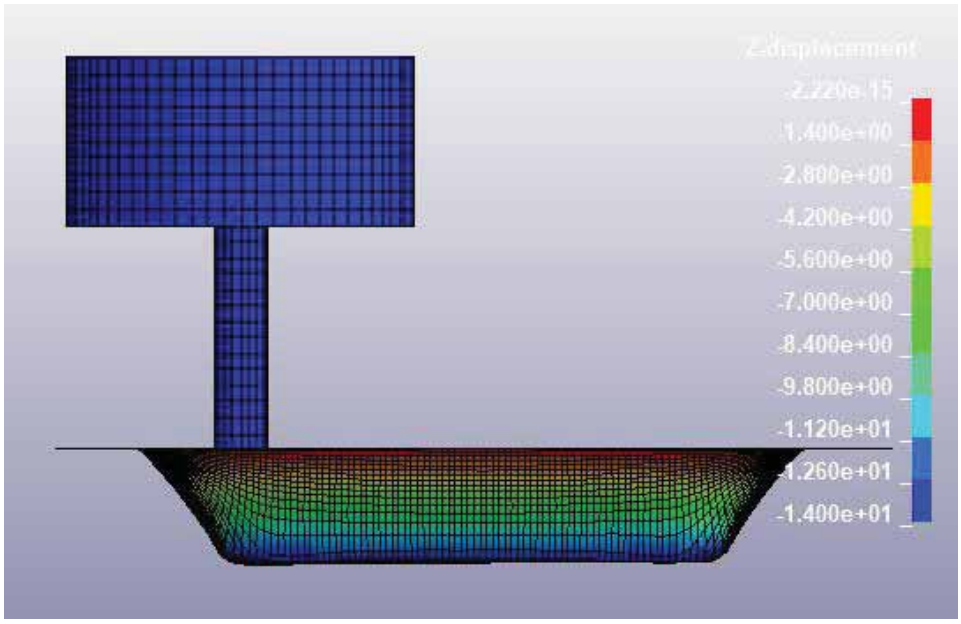

b)

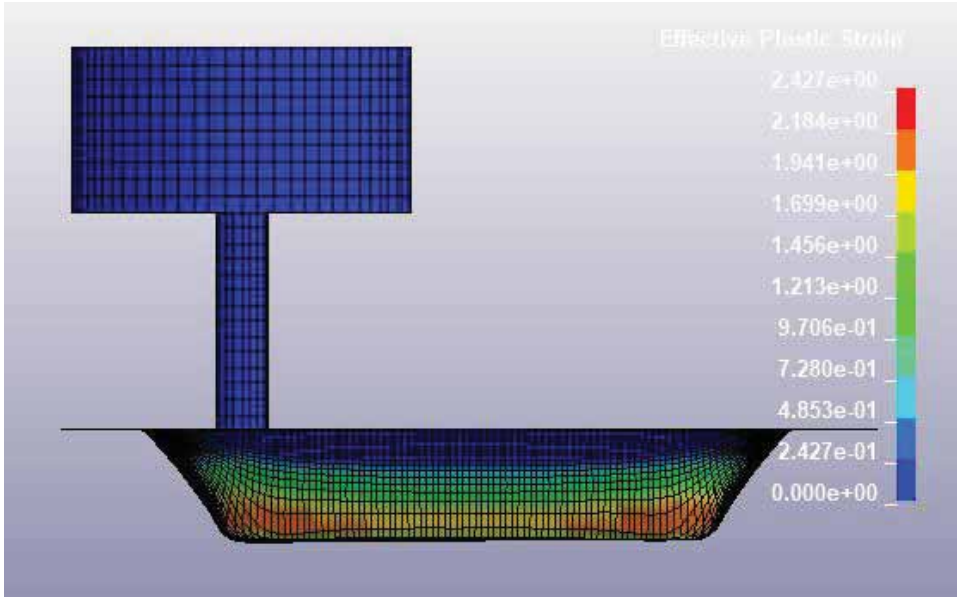

Figure 24. a) VWA with maximum z displacement at depth of fracture. b) Corresponding effective plastic strain for state shown in figure a)

Chapter Four: Results and Discussion

In this Chapter, the results for the Characterization Process, the Uniform Wall Angle and Variable Wall Angle experiments will be presented and discussed. The experimental results of both type of parts will be compared to their respective simulation.

4.1 Characterization Results

Four Tensile Tests were carried out for specimens 2, 4, 5, and 8 with 0°, 45°, 45°, and 90° orientation with respect to the rolling direction of the sheet metal. The resulting Load vs Deformation and analogous True Stress – True Plastic Strain are presented on appendix A in figures 65 through 72.

The results obtained from the tensile tests showed almost equal curves between specimens 4 and 5 which share the 45° orientation, therefore only one of them was used for the subsequent parts of this thesis. Arbitrarily the curve from specimen 5 was chosen.

There is a notable difference between the strain levels achieved between the specimens. Specimen 8 had the greatest true strain of 0.62 followed by sample 2 with 0.524 strain value. Specimens 4 and five, which overlap in Figure 25, have the lowest maximum strain of 0.422. This is due to the maximum travel distance of the extensometer, for specimens 4 and 5 when the extensometer reached its 25 mm travel distance, the tensile test would be immediately terminated by de Universal Testing Machine Control Unit. For Specimens 2 and 8, the test was paused before over-travel of the extensometer occurred and continued using deformation values provided by the Universal Testing Machine.

Therefore, this differences in maximum strain before fracture are only significant between specimens 2 and 8.

The yield stress for each specimen is noted in Table 10. This value is where the trues stress vs strain hardening curve starts, therefore, during the simulation the behavior of the material will be modeled according to the Young's Modulus until the stress experimented by an element reaches the yield stress. After that point the material's behavior will be modeled after the True Stress vs Effective Plastic Strain curve.

Table 10 Yield Stress for each Specimen

Specimen	2	4	5	8
Yield Stress(MPa)	211.63	209.1	208.29	217.53

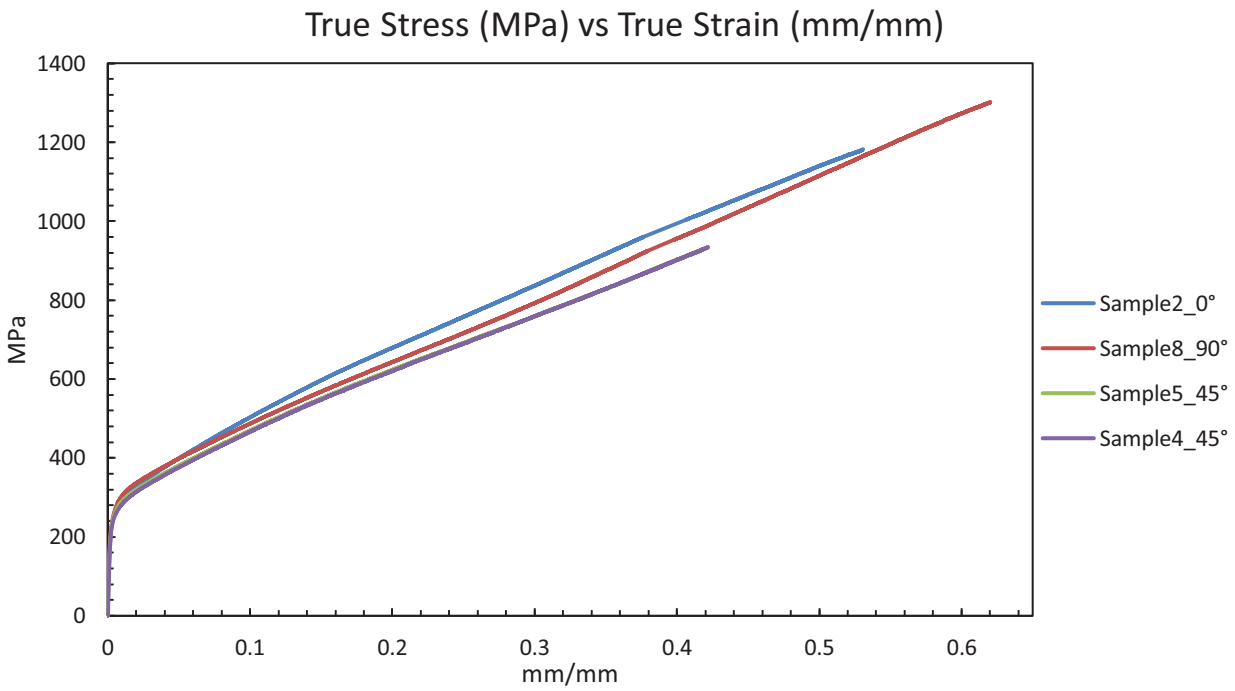

Figure 25. Comparison of True Stress vs True Strain Curves

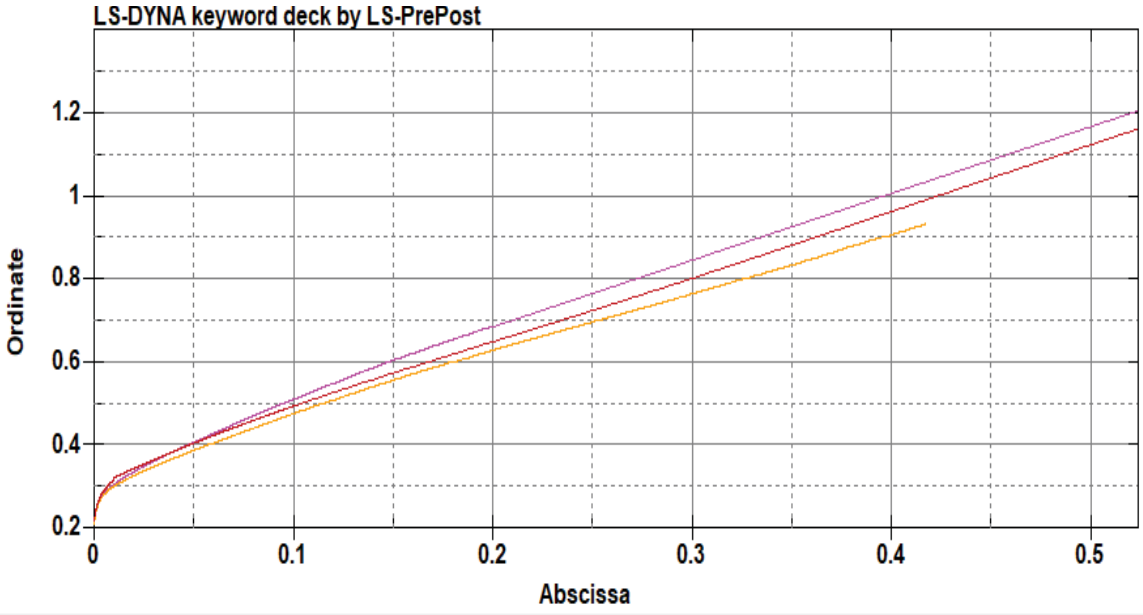

Figure 26. True Stress vs Effective Plastic Strain curves inserted in LS-PrePost; purple 0°, red 90° and yellow 45°

4.2 Uniform Wall Angle (UWA) Results

Three UWA parts were manufactured with the same parameter listed in Table 11. Using those parameters, a simulation using Finite Elements Method was carried out. In total there were 4 simulations, each one using the mechanical properties of Stainless Steel AISI - 304 sheet metal in 0°, 45°, and 90° with respect to its rolling direction.

Table 11 Experimental parameters of the UWA formed parts

Width [mm]	Forming Angle	Step Down [mm]	Number of Steps	Tool Radius [mm]	Spindle Speed [rpm]	Feed Rate[mm/min]	Lubrication Rate
67.4	45°	0.25	80	3.175	1250	500	Every 5 mm

These experiments were performed to determine the influence of anisotropy of the Stainless Steel AISI - 304 sheet metal of 0.45 mm of thickness during the simulations. The following sections depict the experimental and simulation results and a comparison between both to determine the accuracy of the simulation model.

4.2.1 UWA Experimental Results

Three pyramids, P19, P20, and P21, were formed with the parameters depicted in Table 11 and were afterwards 3D scanned to measure the wall angles and thickness along cross sections in the XZ plane and YZ plane as described in Chapter Three on Methodology. The formed pyramids can be seen in Figure 27, Figure 28, and Figure 29.

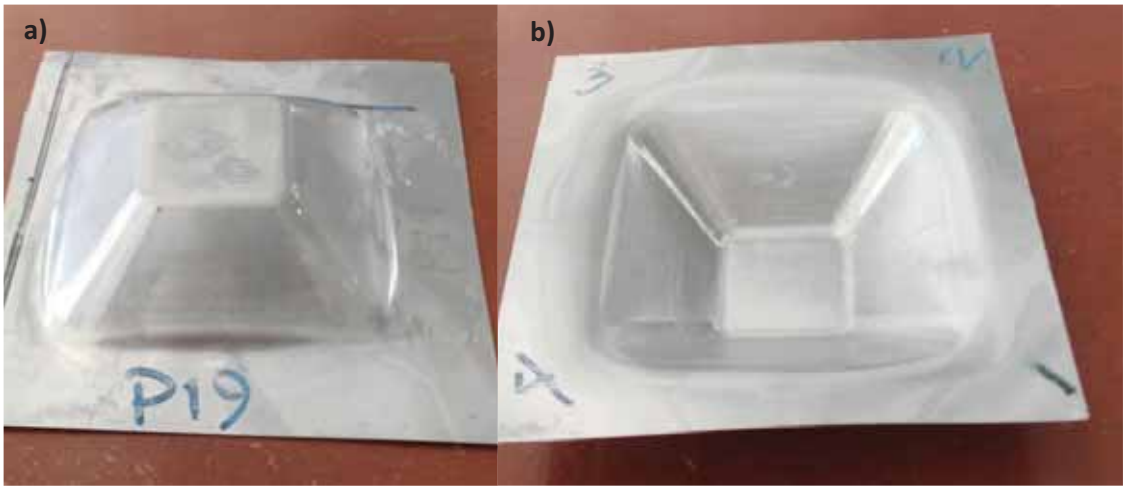

Figure 27. UWA Part P1 9a) downside and b) upside

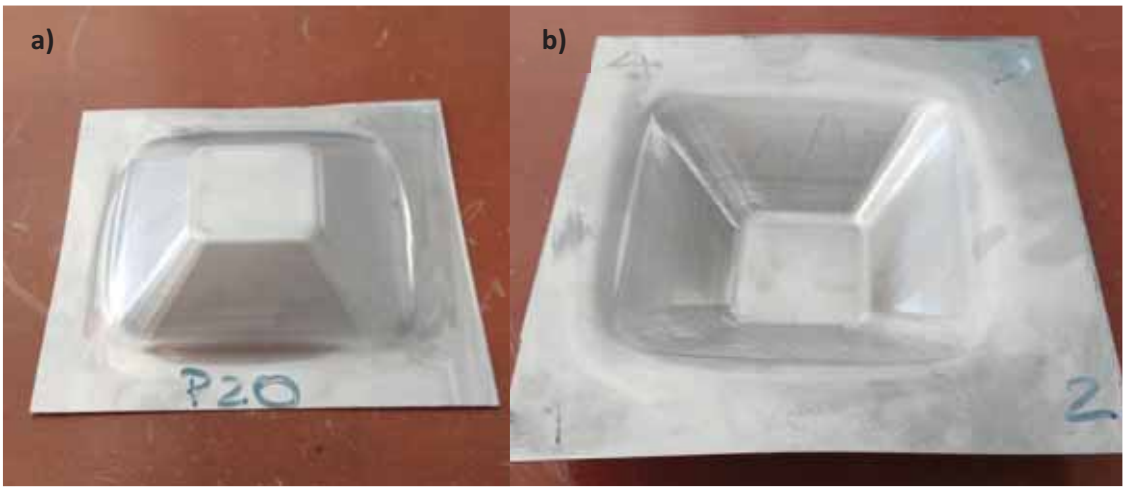

Figure 28. UWA Part P120 a) downside and b) upside

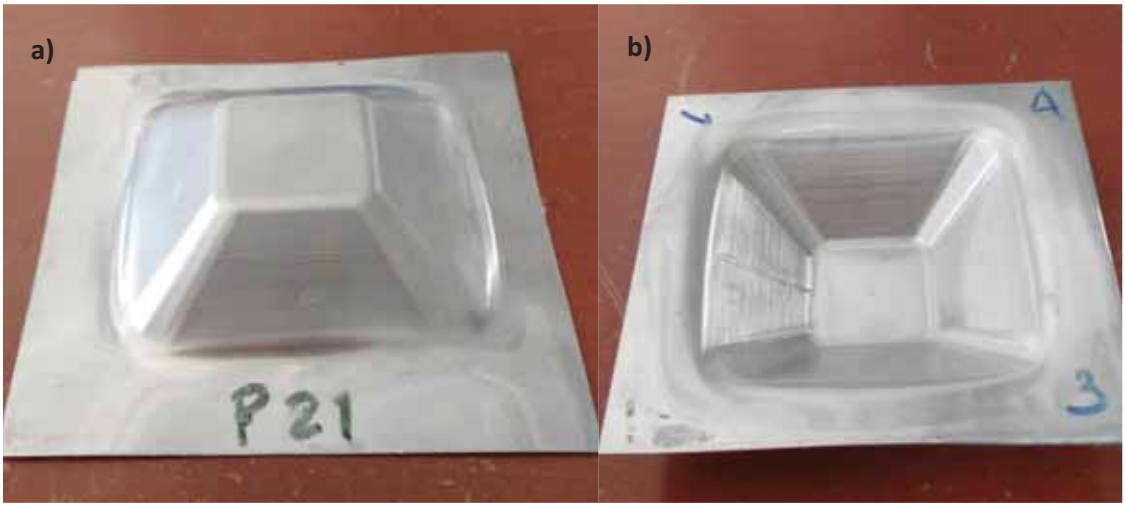

Figure 29. UWA Part P121 upside and downside

The results from the scanning procedure yielded the results shown in the following figures from Figure 30 to Figure 41.

Part P19

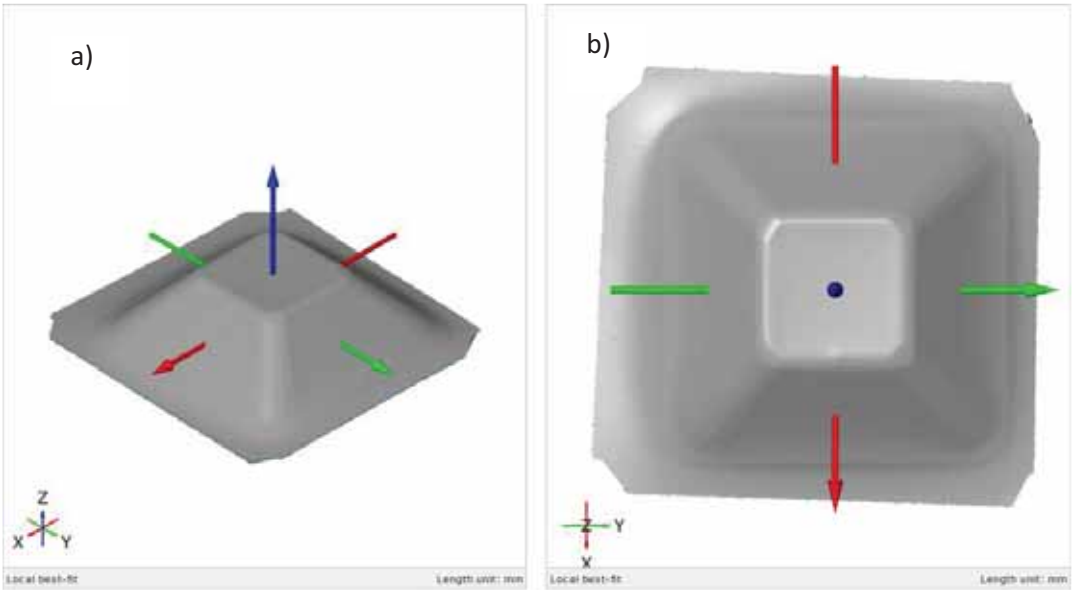

Figure 30. a) Isometric and b) Top View of scanned P19

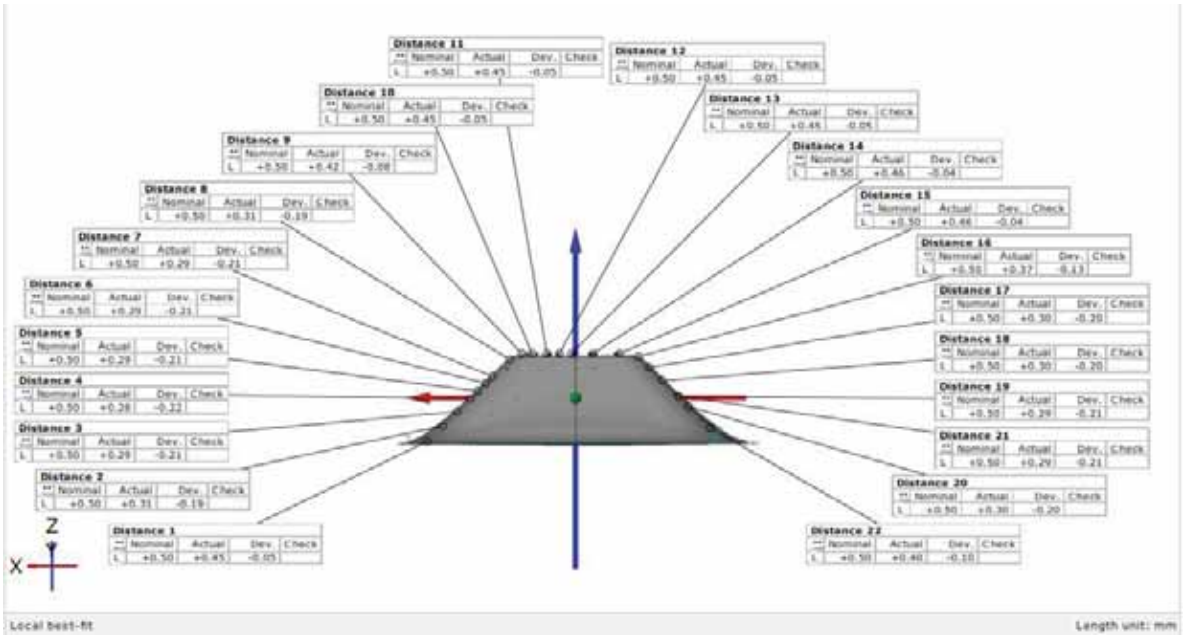

Figure 31. Summary of thickness on XZ plane in mm. Thickness labeled as "Actual"

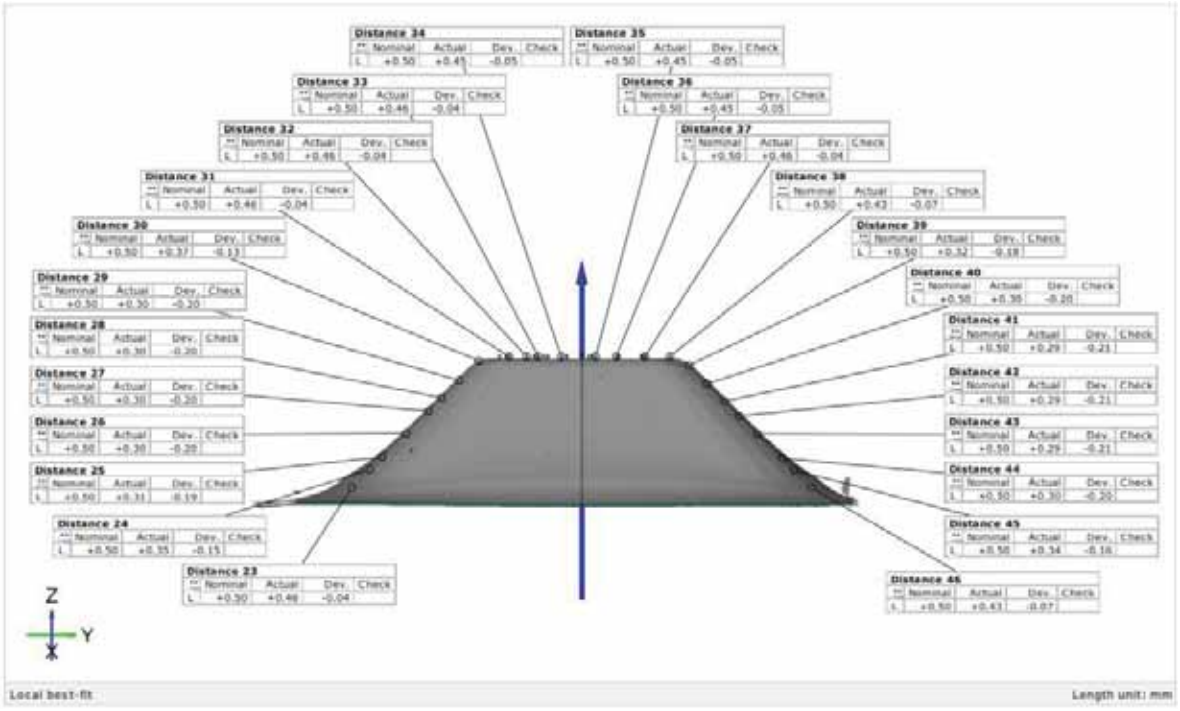

Figure 32. Summary of thickness on YZ plane in mm. Thickness labeled as "Actual"

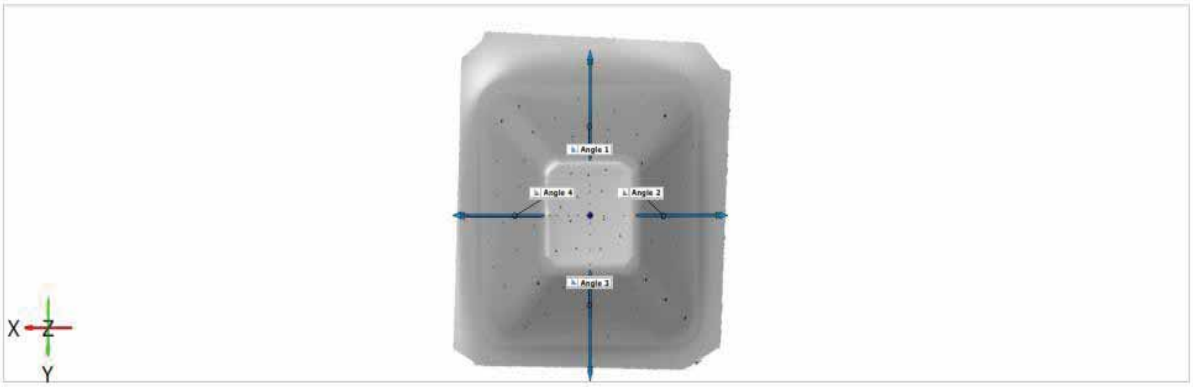

Element	Datum	Property	Nominal	Actual	Tol -	Tol +	Dev	Check	Out
Angle 1		∠	+45.00	+44.58			-0.42		
Angle 2		∠	+45.00	+44.36			-0.64		
Angle 3		∠	+45.00	+44.67			-0.33		
Angle 4		∠	+45.00	+44.21			-0.79		

Figure 33. P19 Measurement of Wall Angles, labeled as "actual"

Part P20

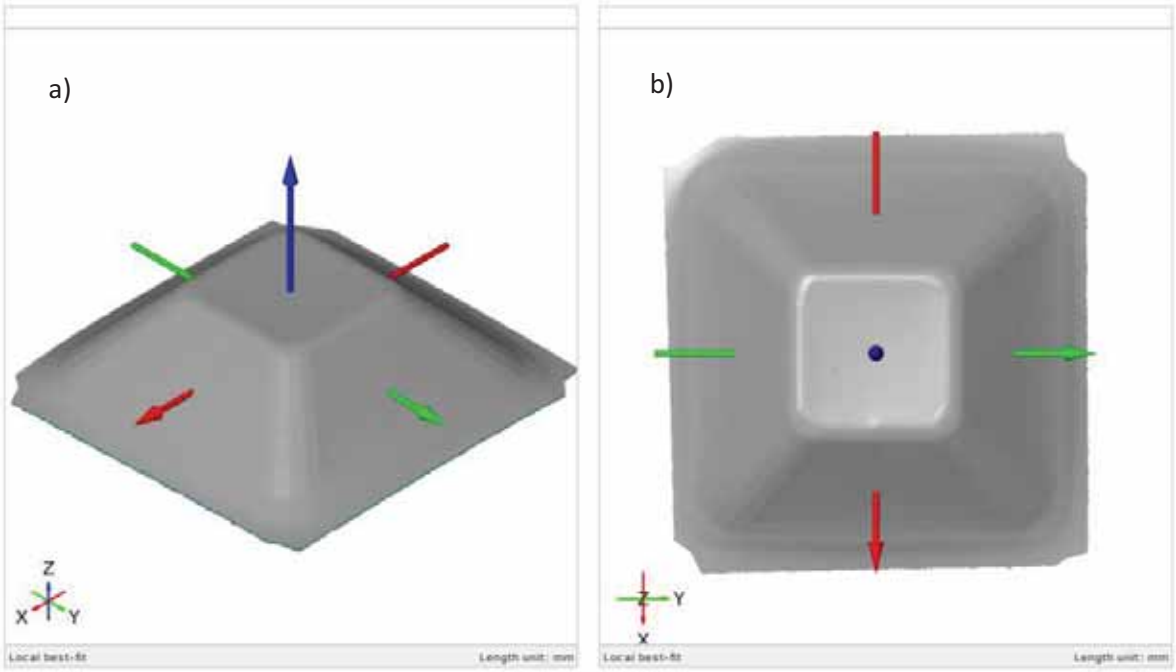

Figure 34. a) Isometric and b) Top View of scanned P20

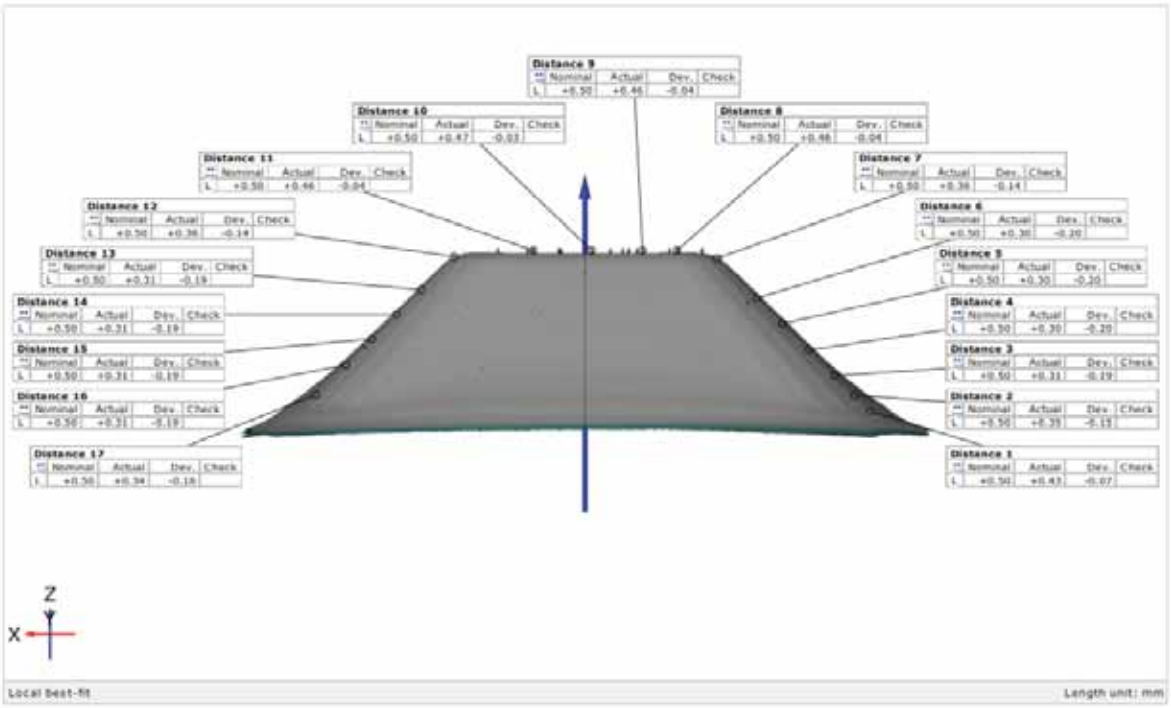

Figure 35. Summary of thickness on XZ plane in mm. Thickness labeled as "Actual"

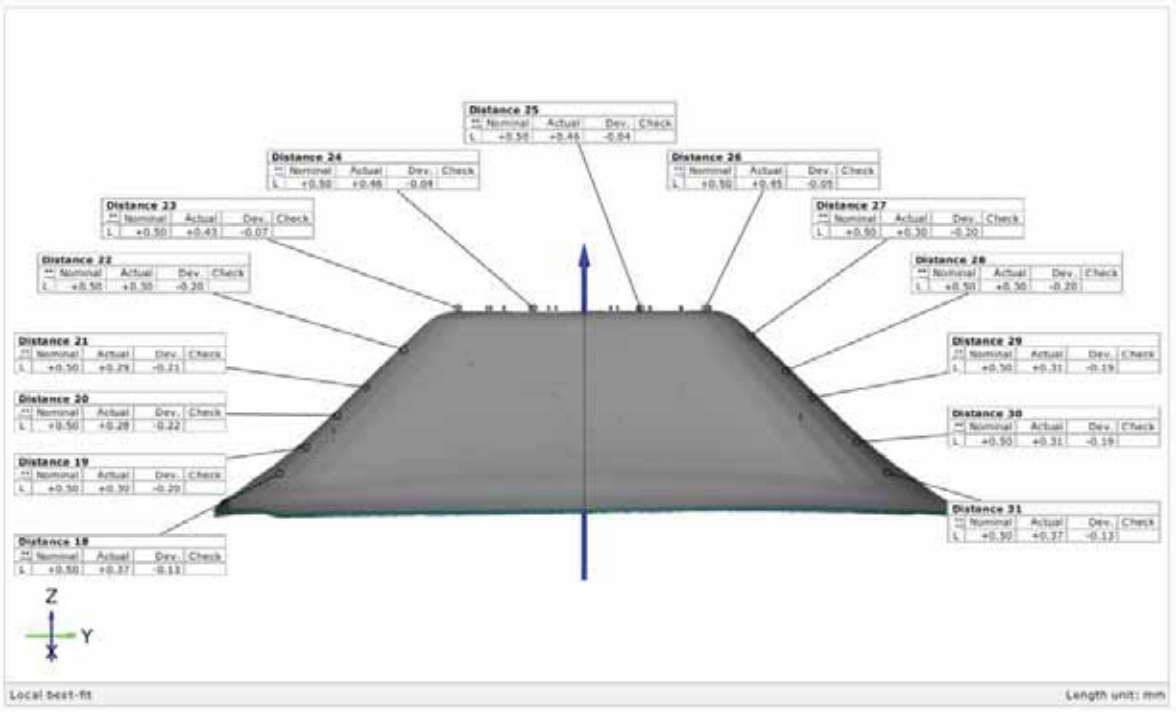

Figure 36. Summary of thickness on YZ plane in mm. Thickness labeled as "Actual"

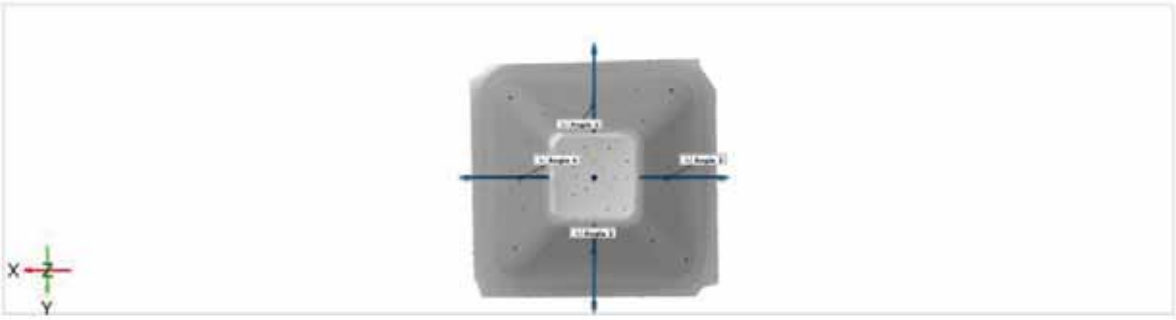

Element	Datum	Property	Nominal	Actual	Tol -	Tol +	Dev	Check	Out
Angle 1		∠	+45.00	+44.06			-0.94		
Angle 2		∠	+45.00	+44.32			-0.68		
Angle 3		∠	+45.00	+44.41			-0.59		
Angle 4		∠	+45.00	+44.15			-0.85		

Figure 37. P20 Measurement of Wall Angles, labeled as "actual"

Part P21

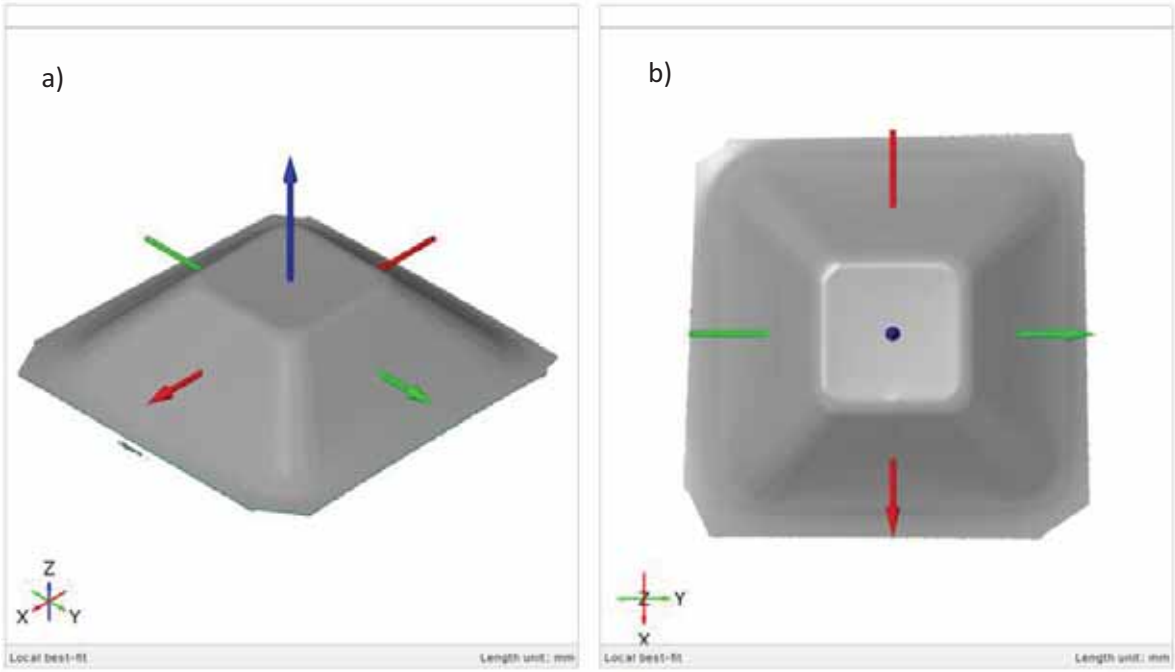

Figure 38. a) Isometric and b) Top View of scanned P20

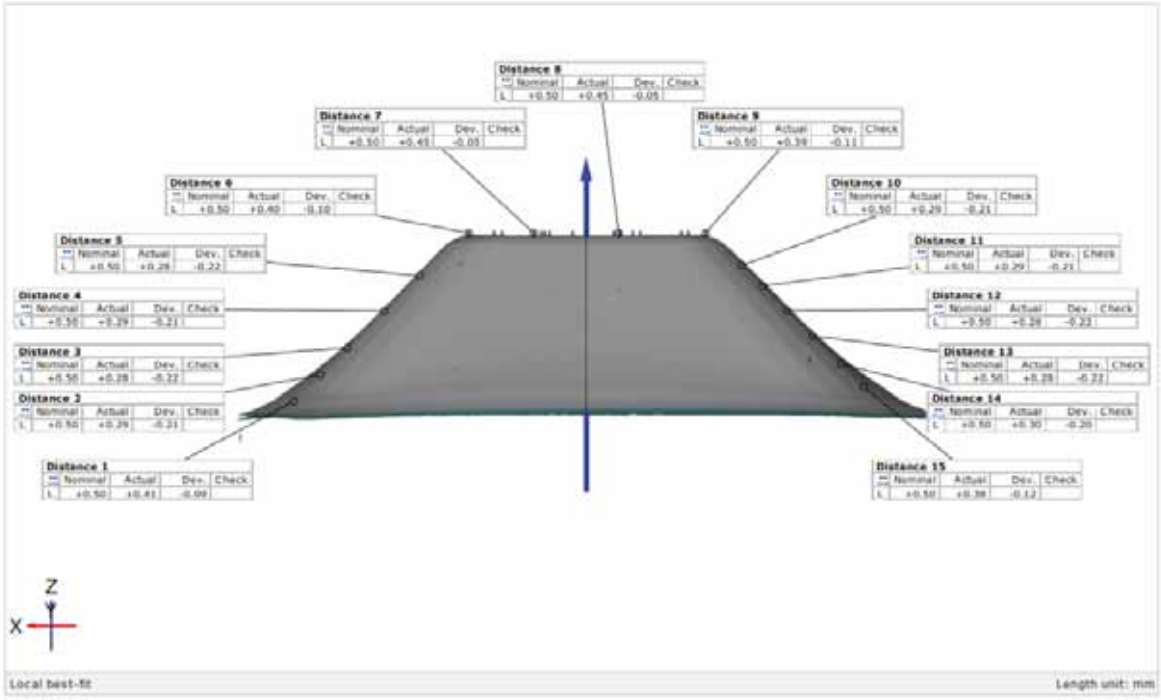

Figure 39. Summary of thickness on XZ plane in mm. Thickness labeled as "Actual"

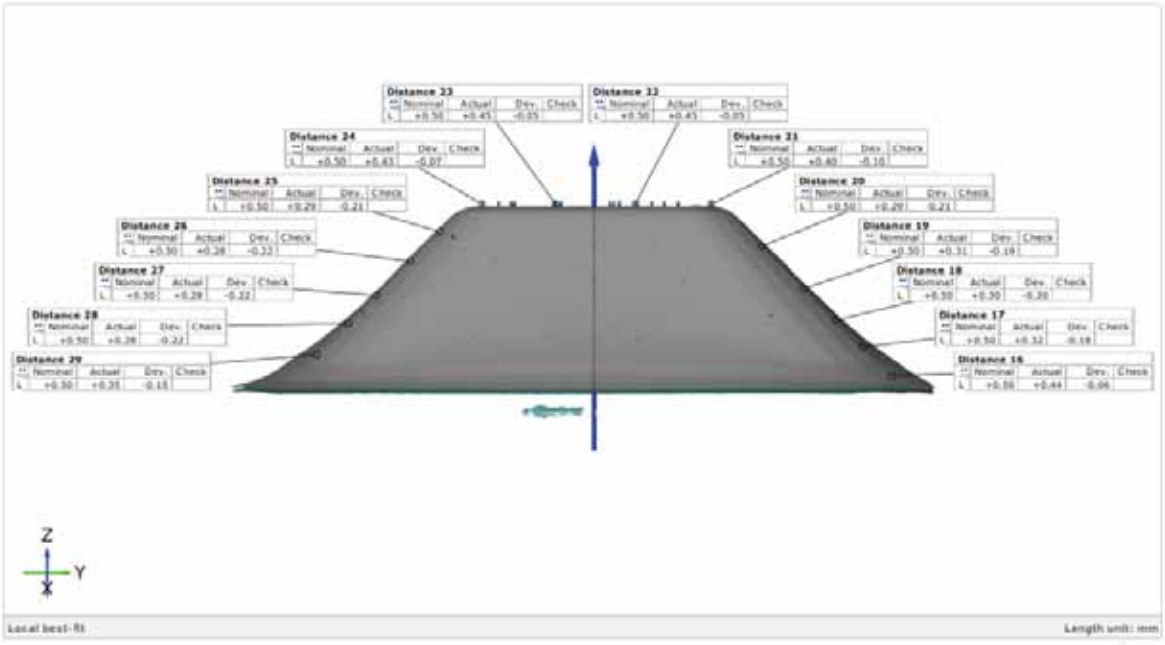

Figure 40. Summary of thickness on YZ plane in mm. Thickness labeled as "Actual"

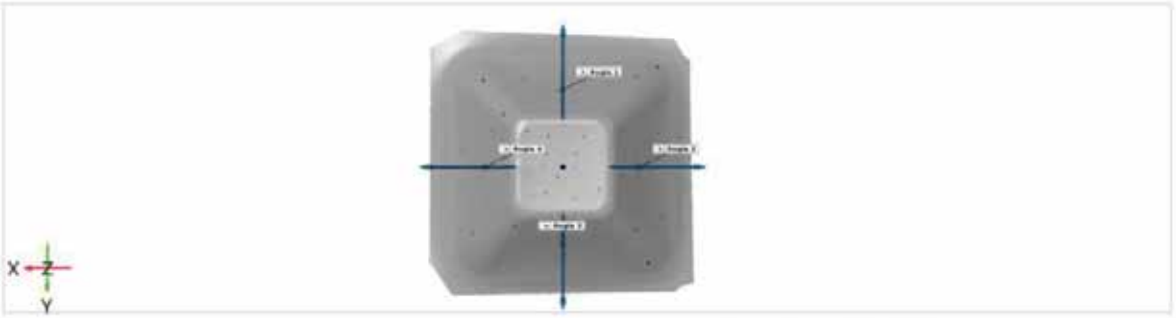

Element	Datum	Property	Nominal	Actual	Tol -	Tol +	Dev	Check	Out
Angle 4		∠	+45.00	+44.73			-0.27		
Angle 3		∠	+45.00	+44.75			-0.25		
Angle 2		∠	+45.00	+44.86			-0.14		
Angle 1		∠	+45.00	+44.78			-0.22		

Figure 41. P21 Measurement of Wall Angles, labeled as "actual"

4.2.2 UWA Simulation Results

Following the steps described in the methodology chapter, curves showing shell thickness vs position along X and shell thickness vs position along Y were obtained by means of Finite Element Analysis simulation. They are presented from Figure 42 to Figure 49.

For each material orientation 0°, 45°, 90°, and "Isotropic Curve" , label used for the plastic behavior defined by the strength coefficient K and the hardening exponent n there is a curve on the XZ cross section (along the X axis) and a curve for the YZ cross section (along Y axis).

0° material orientation:

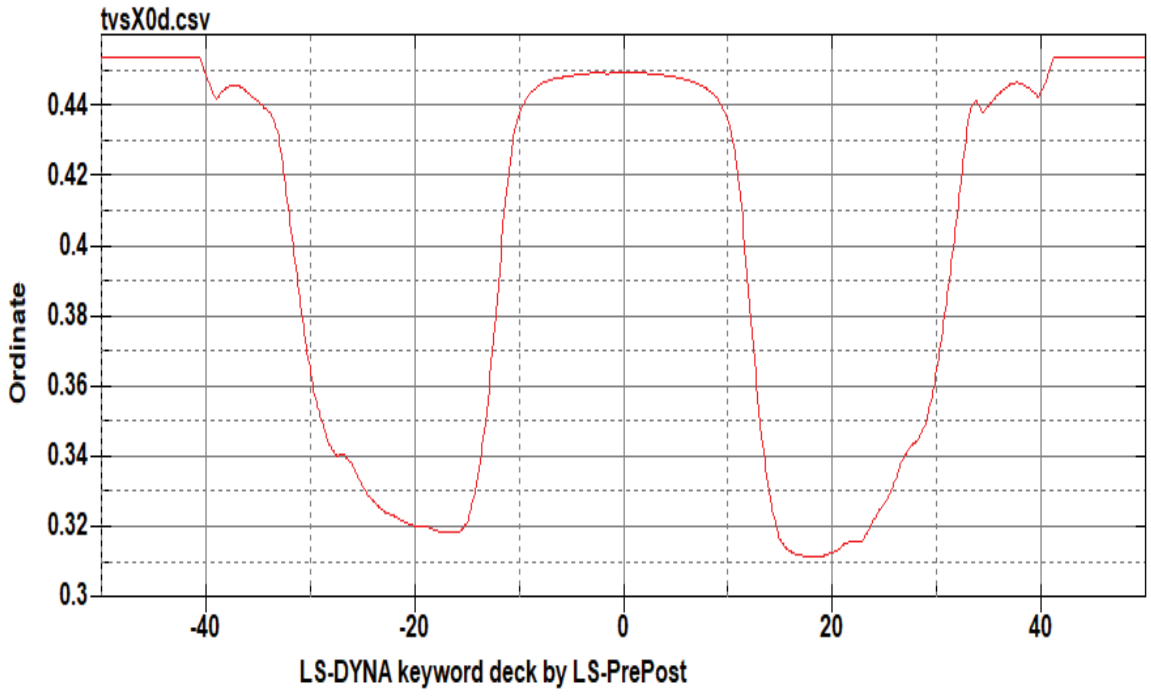

Figure 42. Thickness (mm) vs X position in mm

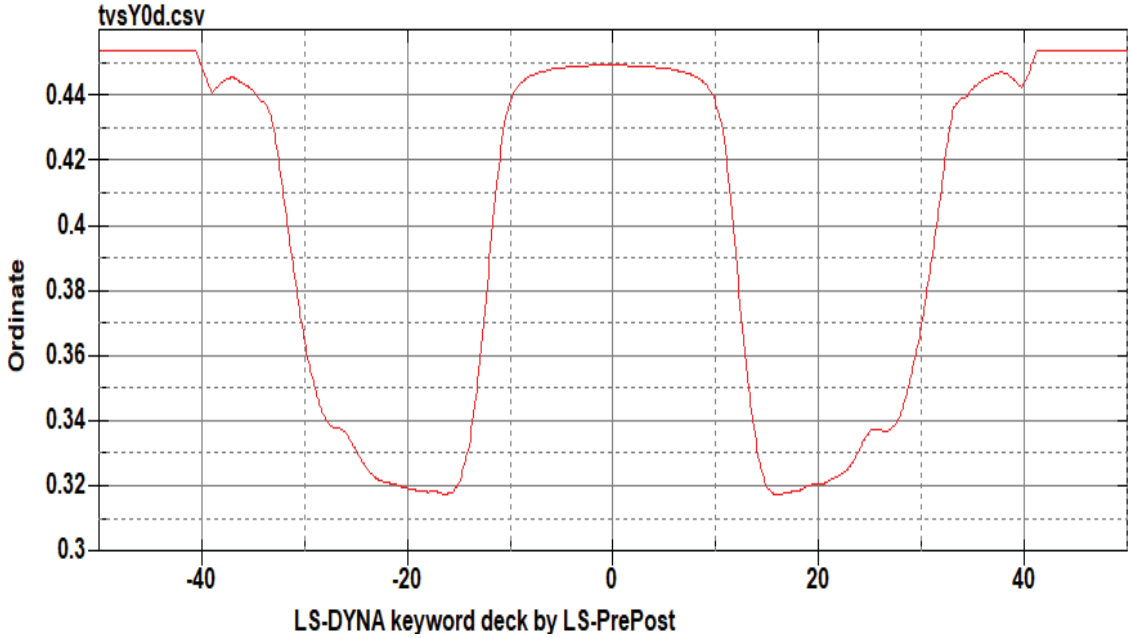

Figure 43. Thickness vs Y position in mm

45° material orientation:

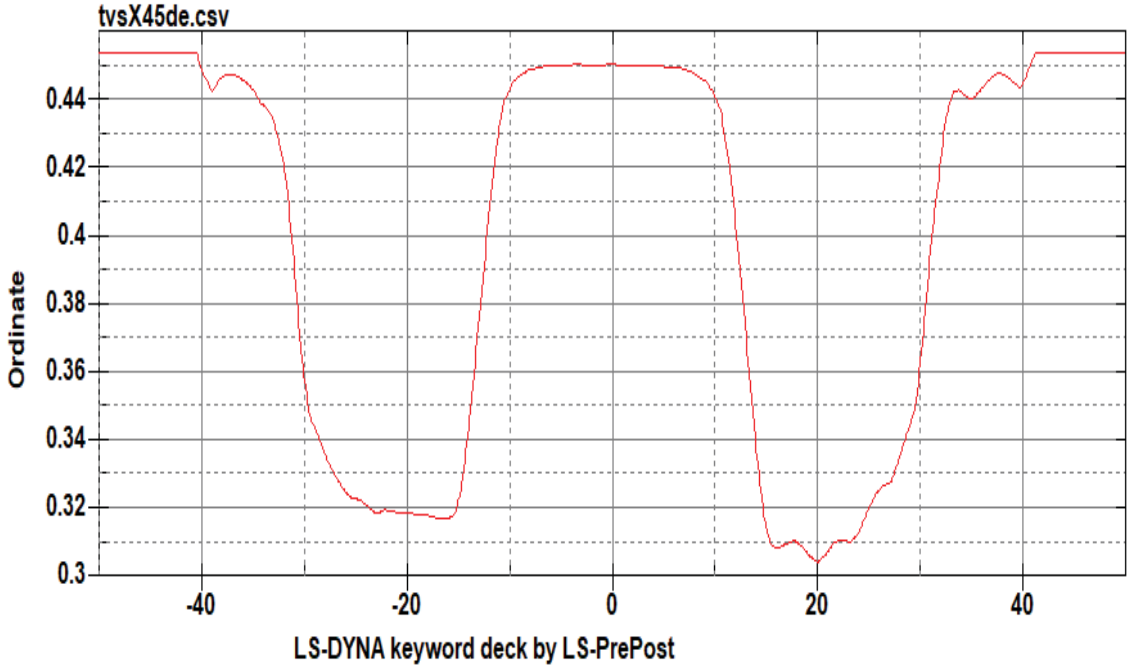

Figure 44. Thickness vs X position in mm

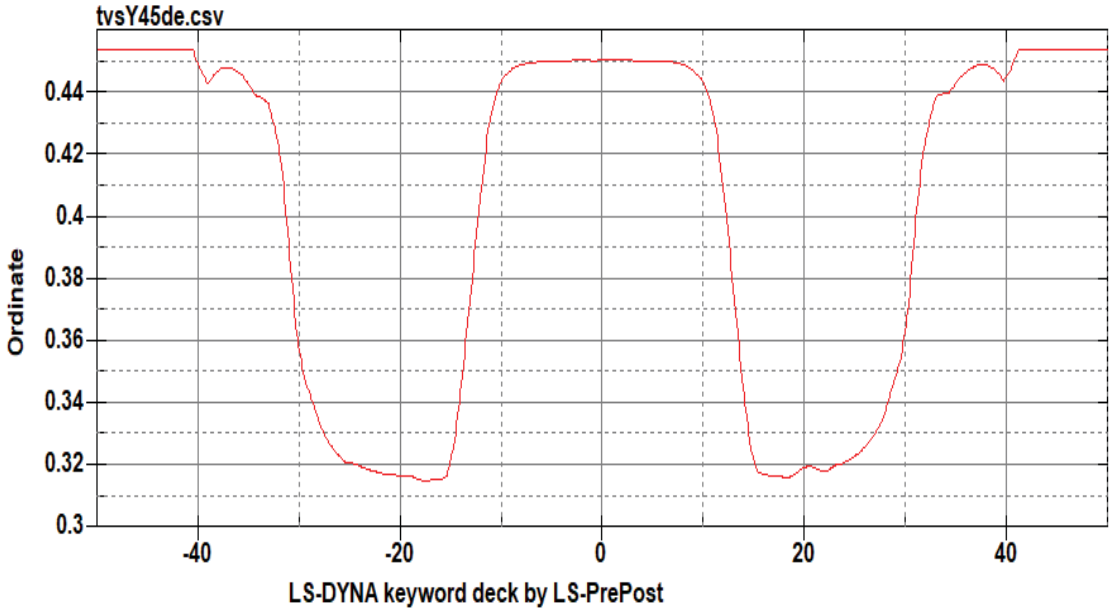

Figure 45. Thickness vs Y position in mm

90° material orientation

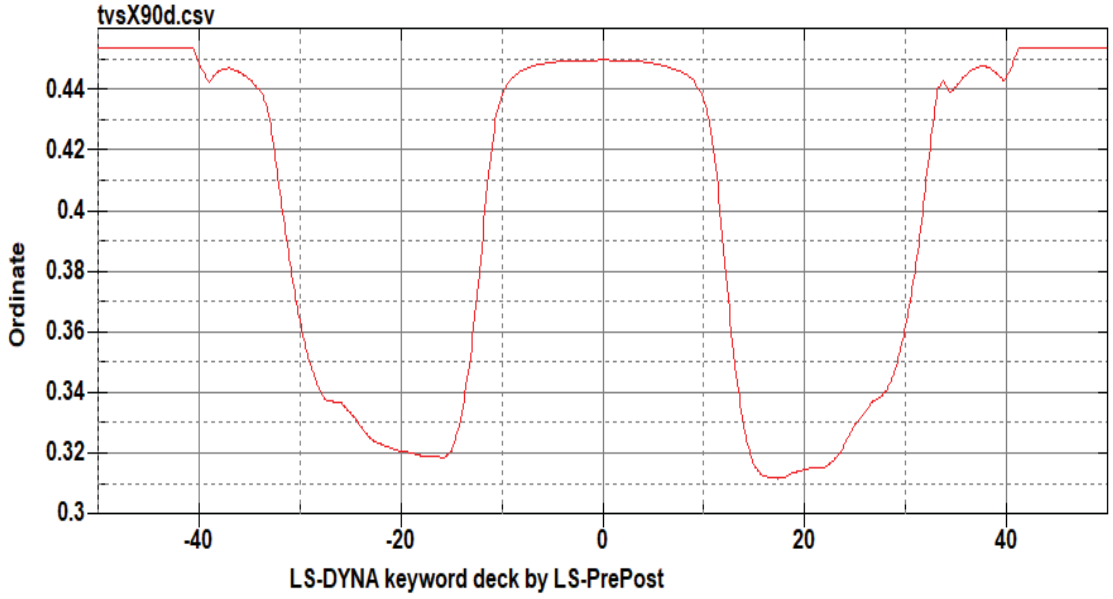

Figure 46. Thickness vs X position in mm

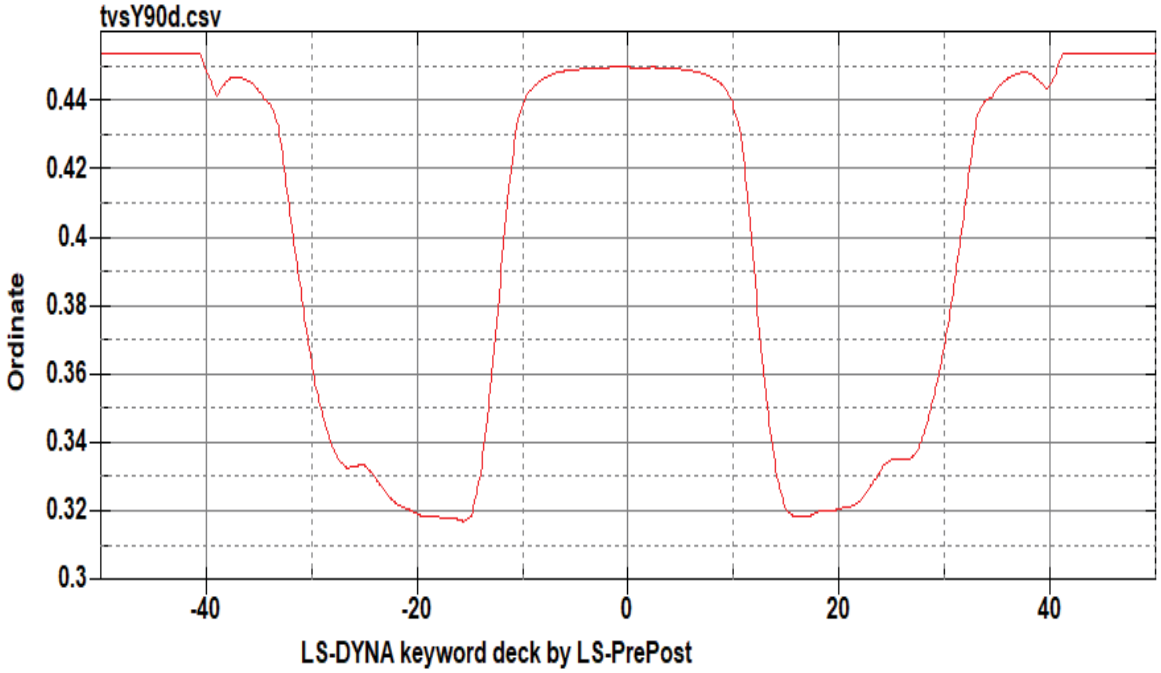

Figure 47. Thickness vs Y position in mm

Isotropic curve (n, K values for plastic behavior instead of true stress strain curve)

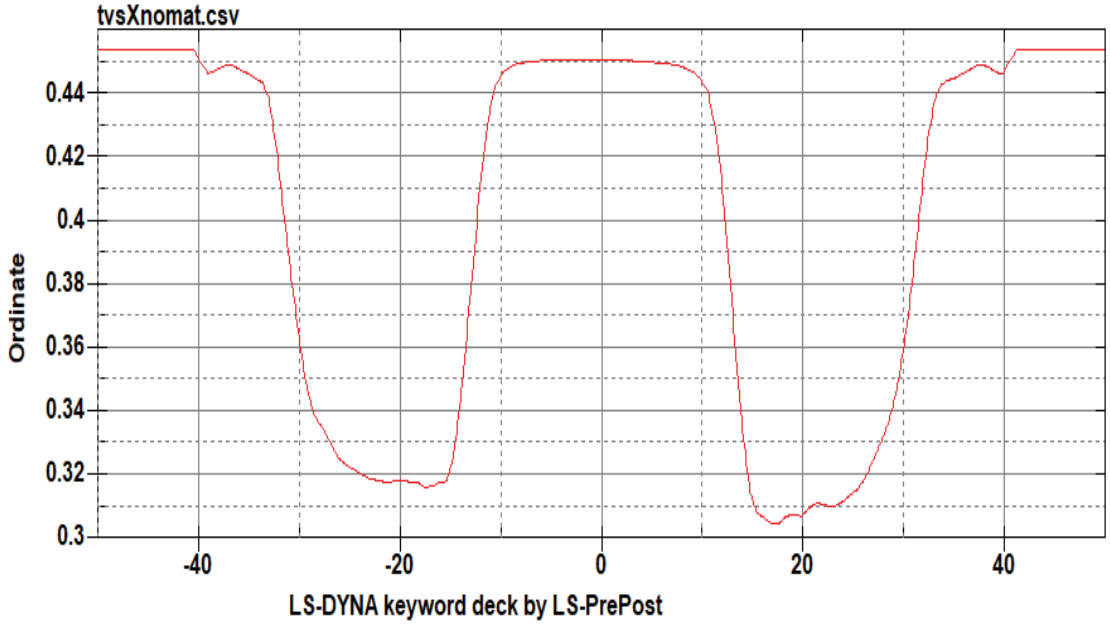

Figure 48. Thickness vs X position in mm

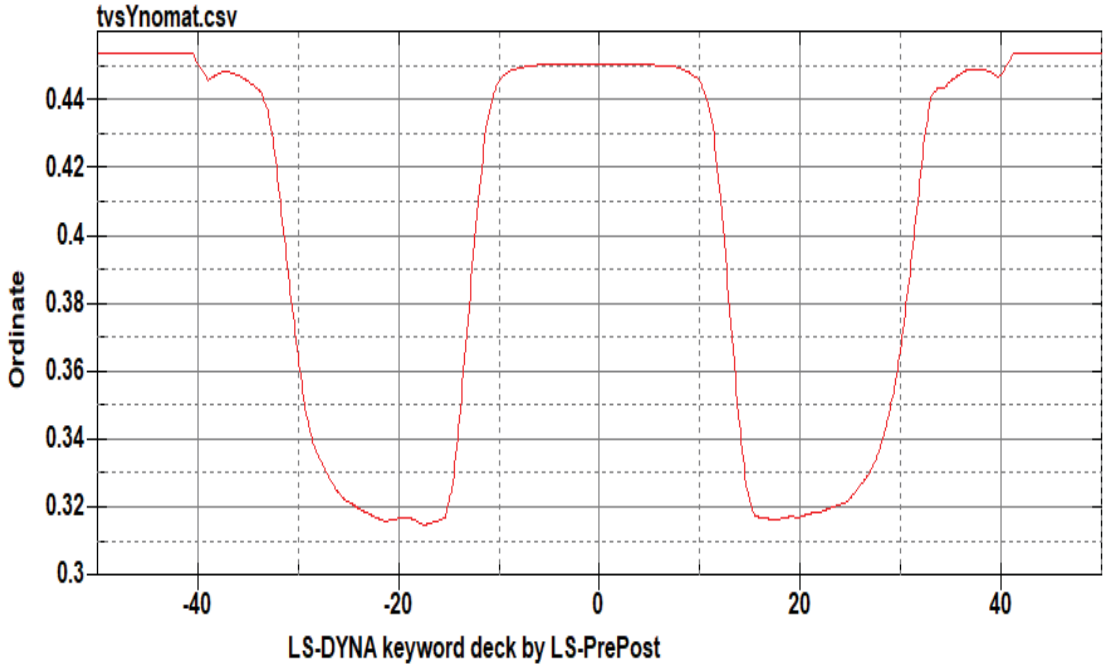

Figure 49. Thickness vs Y position in mm

It is important to observe that in the curves along the X direction, the positive side of the curve has a lower minimum value, meaning that the pyramid is not symmetric in thickness. This is because on the positive X axis is where the tool does the step down during the forming process, causing a slightly higher thinning of the sheet metal. This phenomenon can be seen in Figure 50.

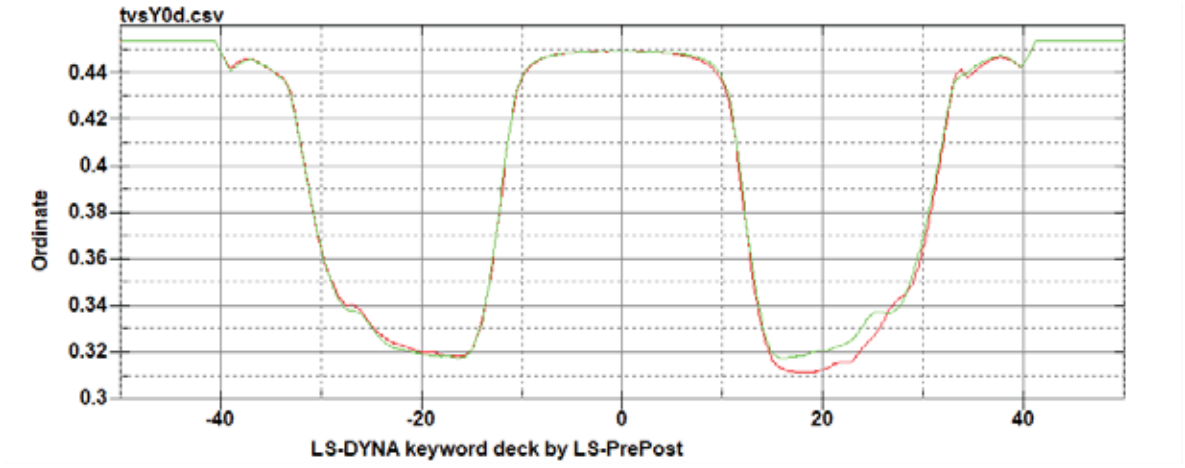

Figure 50. Curves of thickness vs x position and thickness vs y position overlapped. Green along YZ, Red along XZ

On Figure 51, the four curves are placed on the same graph for comparison along the YZ plane since it does not have the singularity described above due to the stepdown.

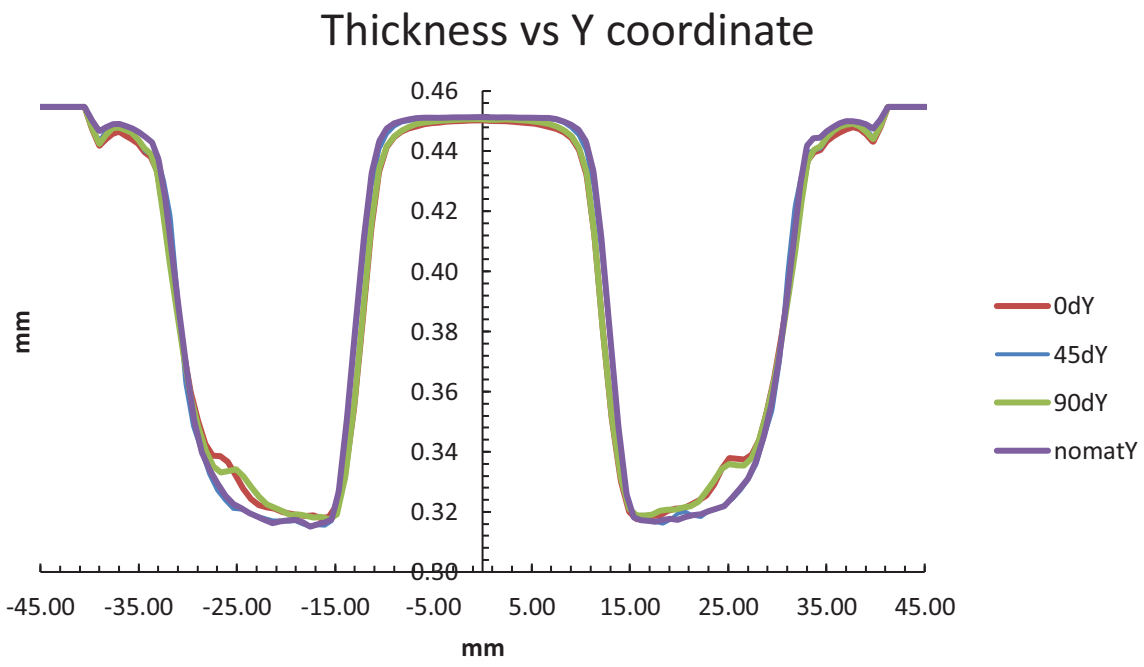

Figure 51. Thickness vs Y coordinate in mm

Figure 52, Figure 53, Figure 54, and Figure 55, depict the measurement of wall angles for each simulation as described in the methodology chapter. Table 12 summarizes the results. The angle shown in the previously mentioned figures is sometimes the supplementary angle of the wall angle.

It can be observed that the angle does not vary significantly due to anisotropy. The biggest difference is between the 90° and 0° simulation and it is a 2.72 % increment from the 0 degrees angle.

Table 12 Summary of Wall Angle Results

Simulation	0°	45°	90	K and n Used "isotropic curve"
Wall Angle	39.846°	40.106°	40.93°	40.598°

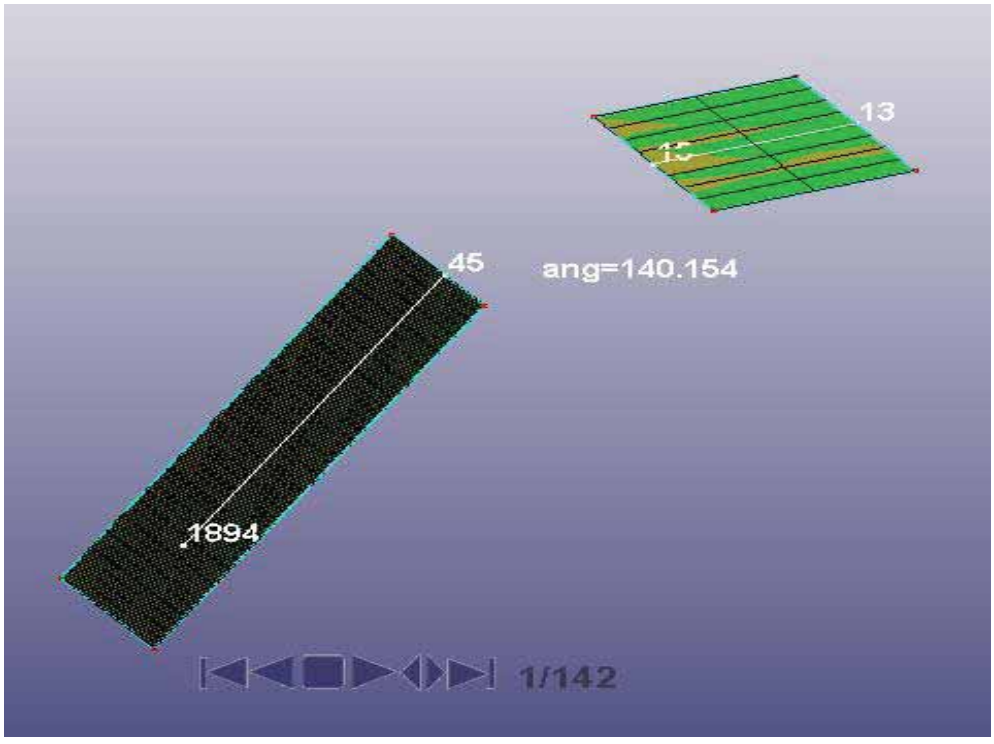

Figure 52. Measurement of Wall Angle using fitted planes for 0° simulation

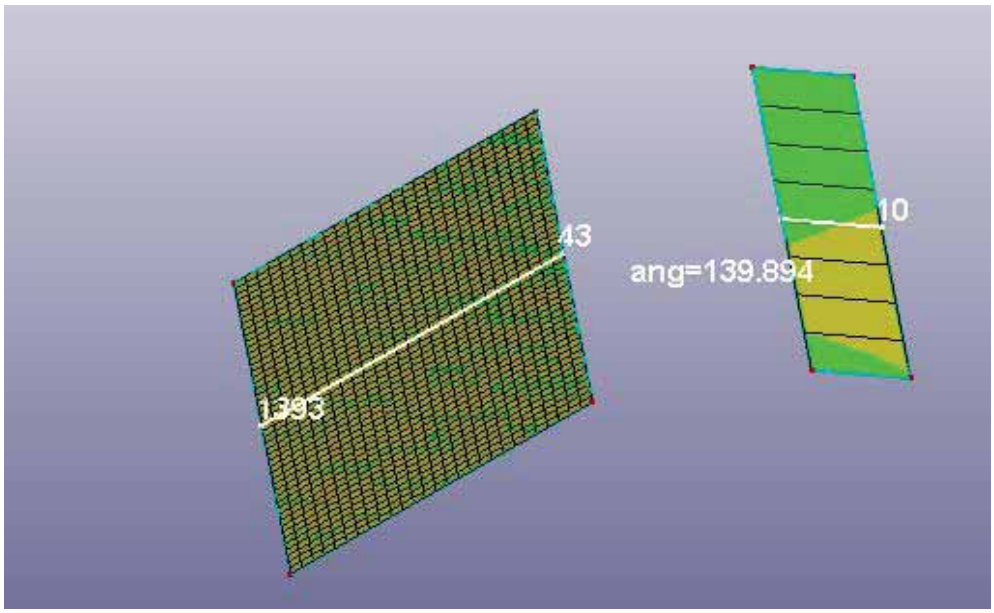

Figure 53. Measurement of Wall Angle using fitted planes for 45° simulation

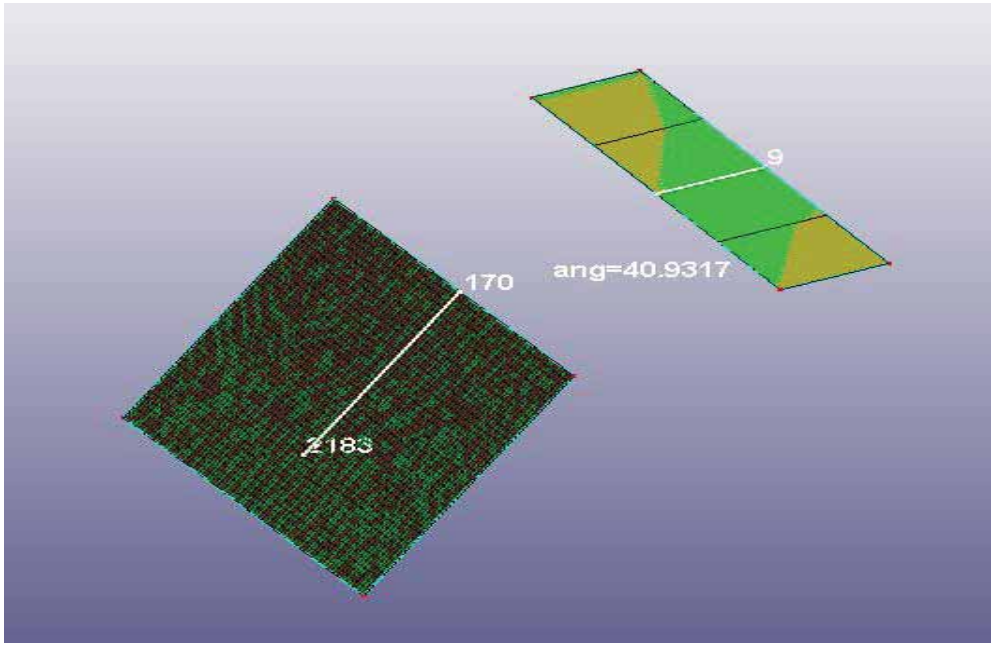

Figure 54. Measurement of Wall Angle using fitted planes for 90° simulation

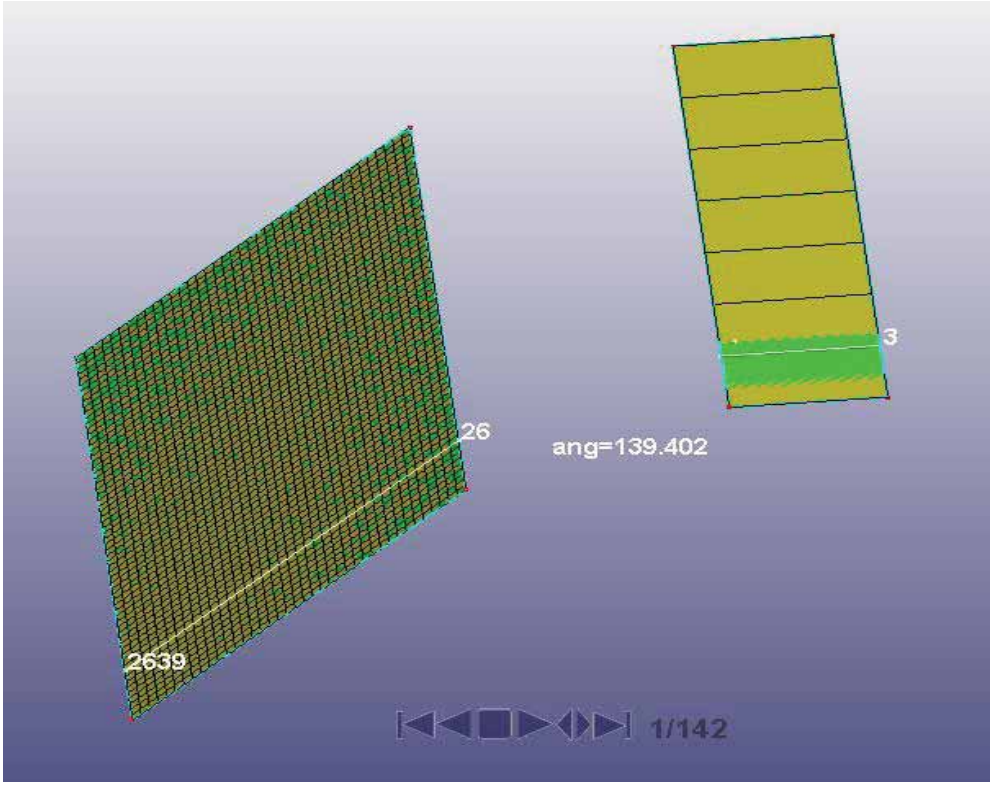

Figure 55. Measurement of Wall Angle using fitted planes for isotropic curve simulation

4.2.3 UWA Experimental and Simulation Results Comparison

4.2.3.1 Thickness Comparison.

The simulation yielded 1000 values of thickness along either the X or Y direction, while the scanning process is more manual and only 51, 55, and 50 points were measured in P19, P20, and P21 respectively.

Therefore, the comparison between the results was done on the x and y coordinates of the experimental results, by finding the appropriate simulation value and subtracting the values. For example, 20y refers to the thickness in pyramid 20p along the y coordinate on the YZ plane. The differences of each pyramid on the experimental measuring point were

compared against the simulation value. The mean difference of thicknesses was calculated for every pyramid on both planes XZ and YZ. Table 13 and Table 14 showcase the mean difference and the standard deviation of the thickness differences for each pyramid compared with each simulation.

Table 13 Mean difference between simulation and experimental thickness.

	0°	45°	90°	"noMat"
19x	0.0100 mm	0.0097 mm	0.0102 mm	0.0094 mm
20x	0.0035 mm	0.0029 mm	0.0036 mm	0.0025 mm
21x	0.0185 mm	0.0187 mm	0.0185 mm	0.0179 mm
19y	0.0050 mm	0.0058 mm	0.0048 mm	0.0060 mm
20y	0.0043 mm	0.0042 mm	0.0042 mm	0.0047 mm
21y	0.0135 mm	0.0132 mm	0.0134 mm	0.0138 mm

Table 14 Standard deviation for values in table 13.

	0°	45°	90°	"noMat"
19x	0.0244 mm	0.0192 mm	0.0242 mm	0.0181 mm
20x	0.0199 mm	0.0141 mm	0.0197 mm	0.0140 mm
21x	0.0267 mm	0.0207 mm	0.0268 mm	0.0196 mm
19y	0.0233 mm	0.0167 mm	0.0235 mm	0.0171 mm
20y	0.0312 mm	0.0271 mm	0.0313 mm	0.0270 mm
21y	0.0256 mm	0.0198 mm	0.0253 mm	0.0201 mm

From the table above, it can be concluded that on the x direction, the model using the values of strength coefficient k and hardening exponent n yields the best accuracy in the simulations,

but for the prediction of thickness across the YZ plane (y direction) the material behaving with the properties of 45° against the rolling direction yields the best results.

Table 15 Average mean difference between the simulation thicknesses against the experimental results.

Pyramid and cross section	19 XZ [mm]	20XZ [mm]	21XZ [mm]	19YZ [mm]	20YZ [mm]	21YZ [mm]
Average mean difference	0.0098	0.0031	0.0184	0.0054	0.0044	0.0135

Table 15 shows that the smallest average mean difference in thicknesses between the simulations and the experiments was found for the part 20p on the XZ plane and the YZ plane. For example, the mean of all the differences in thickness between all the simulations and the experimental values of part P19 across the XZ plane (along the X coordinate) is 0.0098mm.

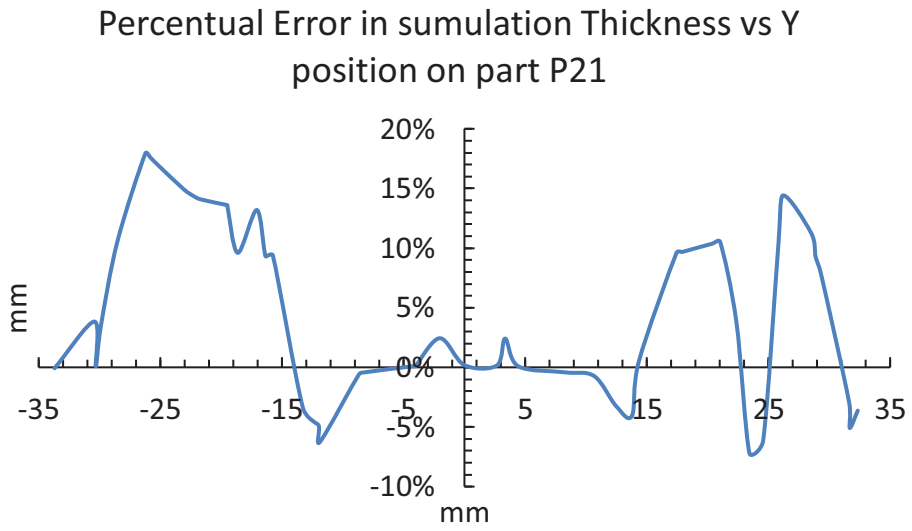

Figure 56. Average percentile Error in Thickness Simulation across the y coordinate of pyramid 21 vs all simulations.

In Figure 56, it is shown that the error in predicting thickness through simulation peaks at around 20%, predicting a thicker sheet than reality. Towards the middle of the graph and the middle of the pyramid, the errors are reduced due to the low deformations experienced in this area. These results on thickness simulation shows that the model needs to be refined to lower the errors and obtain a more representative simulation.

4.2.3.2 UWA part Wall Angle Comparison.

Table 16 and Table 17 show the simulation wall angle results and the experimental wall angle results. As it can be seen, there is a relevant difference between both data. The average simulation angle is 40.37° while the experimental average is 44.488° this means a difference of 4.11° of the averages which is a 9% error on the simulation.

This error is comparable to the one found for thickness, which would fluctuate 0 and 20% having most of the values around 10 %. The source of these errors needs to be investigated further.

Comparing the Simulation results between each other, it can be observed that the value for a material governed by the k and n constants is between the values of 0 and 90°. This in turn suggests that a simulation model that takes the true stress vs hardening for each direction into account at the same time could yield a similar result.

Table 16 Simulated Wall Angle Results

Simulation	0°	45°	90°	K and n Used isotropic curve”
Simulated Wall Angle	39.846°	40.106°	40.93°	40.598°

Table 17 Mean experimental Wall Angles per part.

Part	P19	P20	P21
Average Experimental Wall Angle	44.45°	44.235°	44.78°

4.3 Variable Wall Angle (VWA) Results

4.3.1 VWA Experimental Results

The six pyramids were made obtaining at least one fracture at a single depth, at which point the process was interrupted and the depth noted. An example of the pyramids obtained is shown in **Error! Reference source not found.** where the experiment B3 (VWA2_3) has a s mall fracture that is circled for easier identification.

The results of the six experiments are noted on

Table 18 in which both the depth at fracture and the corresponding angle can be seen. Please note that the drastic difference between the depth of experiments from sets A and B is given by the change in the Generatrix Radius.

a) (b

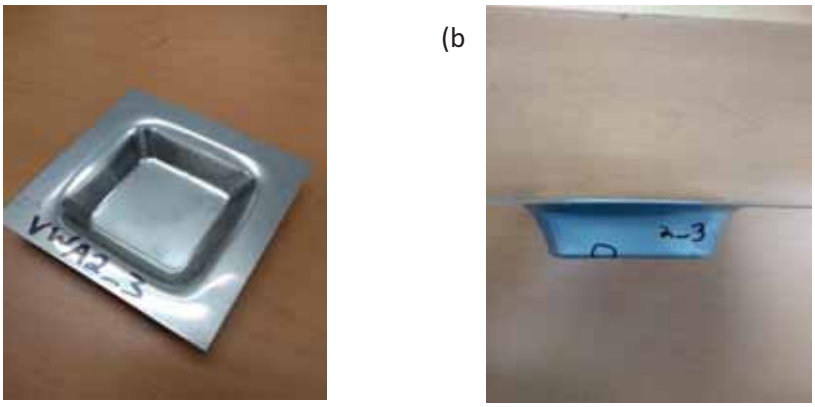

Figure 57. a) Pyramid of Variable Wall Angle of experiment B3 b) front view with circled fracture.

Table 18 Depth and Angle at Fracture of the formability experiments.

Experiment	Generatrix Radius [mm]	Z coordinate (depth) at Fracture [mm]	Angle at Fracture
A1	35	-12.25	76.24°
A2	35	-14.25	79.58°
A3	35	-14	79.17°
B1	50	-20.75	80.29°
B2	50	-20.75	80.29°
B3	50	-20.50	80.00°
			Average = 79.26°

Furthermore, on Table 19 the average depth and angle for each experiment set is denoted. Note that even though there is a clear difference between the average angle of set A and set B, said difference represents only a 2.38% increase.

Table 19 Average Depth and Angle at Fracture for each Experiment Set

Experiment Set	Average Depth at Fracture	Average Angle at Fracture
A	-13.5mm	78.33°
B	-20.67mm	80.19°

The figures from Figure 58 to Figure 63 show the pyramid frusta of variable wall angle that were produced.

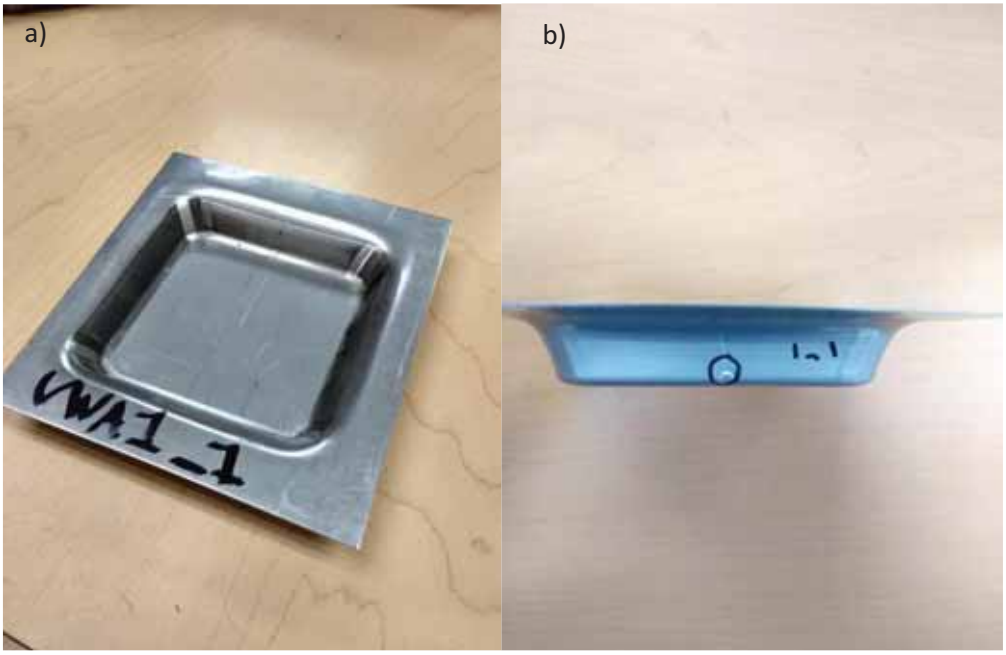

Figure 58. a) Pyramid Frusta A1 b) circled fracture

Figure 59. a) Pyramid Frusta A2 b) circled fracture.

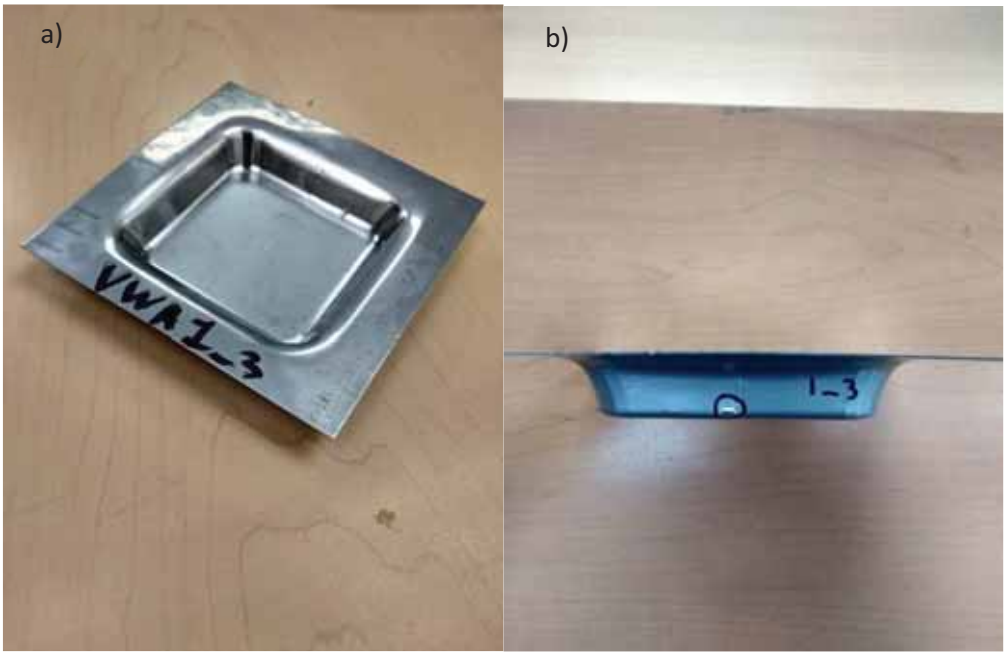

Figure 60. a) Pyramid Frusta A3 b) circled Fracture.

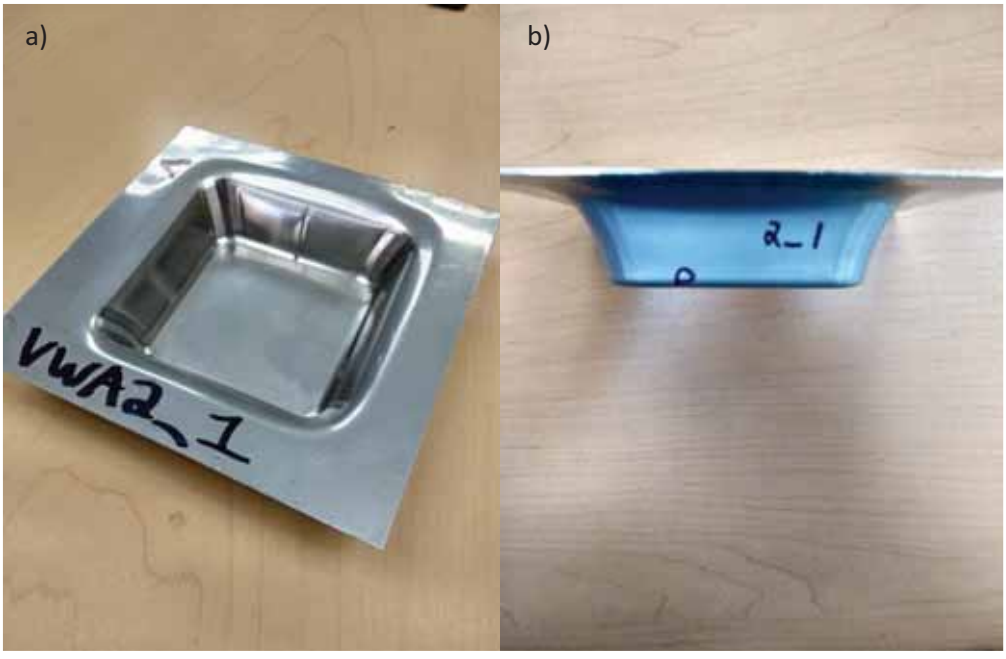

Figure 61. a) Pyramid Frusta B1 b) circled Fracture.

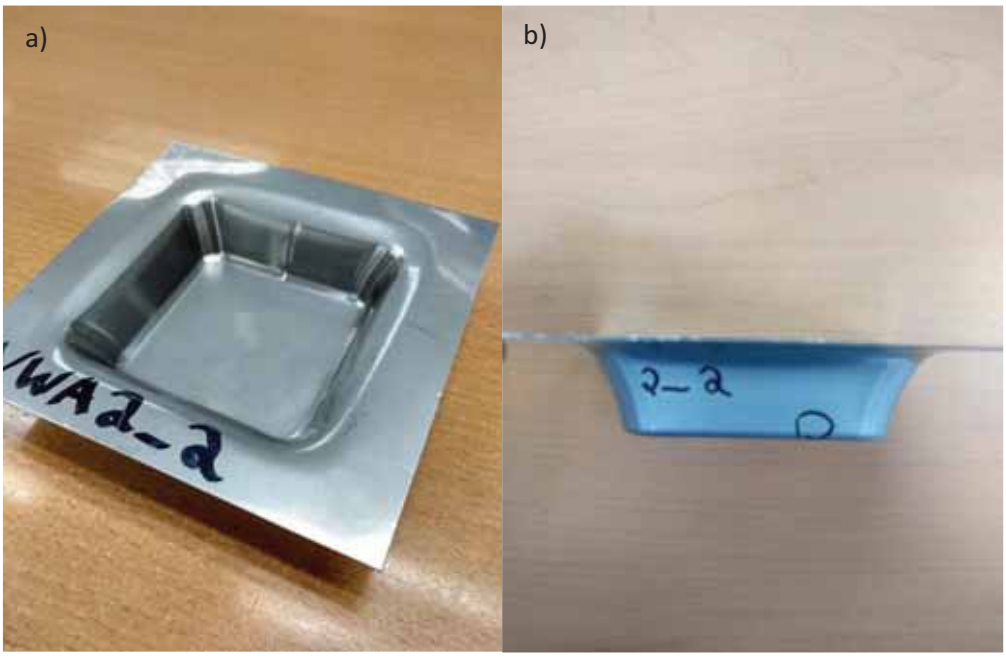

Figure 62. a) Pyramid Frusta B2 b) circled Fracture.

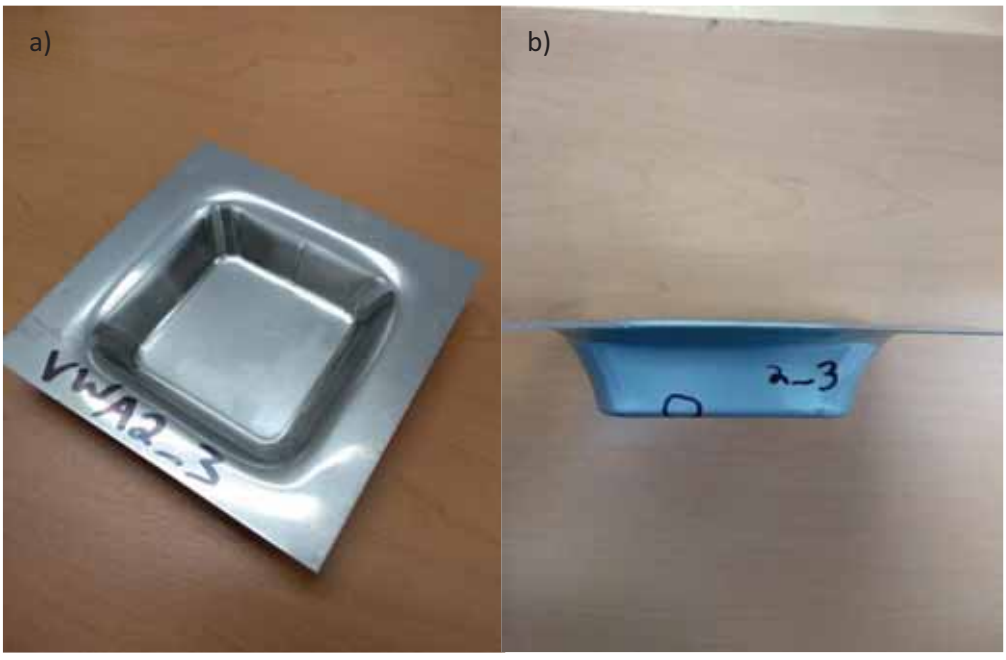

Figure 63. a) Pyramid Frusta B3 b) circled Fracture.

As it was mentioned before, the increase in maximum wall angle between experiment set A and experiment set B is of 2.38%, while the increase in generatrix radius from 35mm to 50mm is of 42.86%. With such few data it is difficult to conclude whether there is a relationship between both parameters. Although, finding the lower limit of the maximum wall angle should be of higher interest in order to prevent failure before it is expected.

The work done by Centeno *et al*. (2014) with Stainless Steel AISI - 304 and various tools diameters gives us a benchmark to which compare the results found in the present chapter. In Table 20, the final forming angle is presented next to the final depth, step down, and tool diameter used.

Table 20 Series of SPIF tests on Stainless Steel AISI - 304 (S=1000rpm) (Centeno, Bagudanch, Martinez-Donaire, Gracia-Romeu, & Vallellano, 2014)

Tool diameter Dt (mm)	**Step down ΔZ (mm/pass)**	**Final depth Z_f (mm)**	**Final forming angle α_f (°)**
20	0.2	22.8/23.0/23.8	68.3 / 68.6 / 68.9
20	0.5	24.5/24.5/24.5	70.9 / 70.9 / 70.9
10	0.2	29.2/28.6/29.0	78.2 / 77.0 / 77.6
10	0.5	29.0/28.4/28.6	77.6 / 78.3 / 77.6
6	0.2	28.3/28.4/28.6	77.0 / 76.7 / 77.0
6	0.5	28.5/28.5/28.5	76.9 / 76.9 / 76.9

A possible reason for the increase in formability, i.e. maximum wall angle, can be due to the difference in depth of both pyramids. A smaller generatrix radius means the change in the angle is more accentuated, and therefore the final angle is reached faster. This can be exemplified by the maximum depth with a 35 mm generatrix of 14.25 mm against a depth of 20.75 mm for the 50 mm generatrix. Since the step down is constant, a bigger depth implies a longer process that means more time for the blank to be heated with the intrinsic friction of

the SPIF process. It is well documented by Gupta and Jeswiet (2017) that a higher temperature increases formability.

Nonetheless, the increase difference is not of significant magnitude, and even the smallest value (76° for experiment A1) represents a high formability compared to other materials evaluated by several researchers as it can be seen in Table 21 where maximum angle, FLDo and thickness are shown.

Table 21 A list of materials with initial thickness and maximum draw angles (Jeswiet & Micari, 2005).

Material	Θmax [degrees]	FLDo	t_0,mm
AA 1050-O	67.5	2.305	1.21
AA 6114-T4	60	0.841	1.0
Al 3003 – O	78.1		2.1
Al 3003 – O	72.1		1.3
Al 3003 – O	71	3.0	1.21
Al 3003 – O	67		0.93
Al 5754 – O	62		1.02
Al 5182 – O	63		0.93
AA 6111-T4P	53		0.93
DC04, mild steel	65	1.2	1
DDQ	70	2.718	1.0
HSS	70	2.718	1
HSS	65	1.924	1
Copper	65	1.808	1
Brass	40	0.701	1

Furthermore, in Table 21, the initial thickness for the various materials is denoted, and it is evident that the thickness used in the experiments of the present work, 0.45 mm, is considerably smaller than those found in the table. As it was mentioned in more detail in the review of literature, a smaller thickness in the sheet metal has been found to represent a decrease in formability (Hirt, Ames, Bambach, & Kopp, 2004). This relationship implies that

for a thickness similar to those in the aforementioned table, the maximum wall angle for Stainless Steel AISI - 304 could be even higher.

As Jeswiet *et al*. has expressed, "Knowing the parameter φmax for a material at a specific thickness, a designer can take the first step in deciding if a sheet metal part can be made in one pass without tearing, or if a two pass or multiple pass sequence should be used…" (Jeswiet & Micari, 2005). The drawing limit for Stainless Steel AISI - 304 for a sheet of 0.45 thickness is not readily available in the current literature, so finding an approximate value for this parameter can aid future Stainless Steel AISI - 304 part designers considering SPIF for their production.

Also, it is to be noted that the fractures were located always above the Fracture Forming Line (Figure 64), the last line formed, this means that the fracture always occurred to the side of the hemispherical tool instead of under it. Similar results were found by other authors Stainless Steel AISI - 304 was also used, they found that this was the case for their experiments with lower tool diameters of 10 and 6 mm (Centeno, Bagudanch, Martinez-Donaire, Gracia-Romeu, & Vallellano, 2014), which are in the range of this work which used a tool diameter of 6.35mm.

Figure 64. Detail Image featuring the fracture of a VWA part

4.3.2 VWA Simulation Results

For Variable Wall Angle parts, the simulation was used to find the maximum effective strain at which the fractures might have occurred. For a more detailed description of this process refer to the methodology chapter.

A summary of the results is provided in Table 22 and in Table 23 for experiment set A and B respectively. The effective plastic strain is taken from each simulation at the fracture height, including the simulation for the material's plastic behavior defined by the strength coefficient k and hardening exponent n of Stainless Steel AISI - 304.

Table 22 Simulated Effective Plastic Strain for experiment set A

Experiment	Depth at Fracture	Simulation Material Orientation	Effective Plastic Strain at Fracture
A1	12.25 mm	0°	2.119
		45°	3.409
		90°	2.134
		Isotropic Curve	2.7
A2	14.25 mm	0°	2.529
		45°	3.794
		90°	2.524
		Isotropic Curve	3.263
A3	14 mm	0°	2.529
		45°	3.794
		90°	2.4465
		Isotropic Curve	3.155

Table 23 Simulated Effective Plastic Strain for experiment set B

Experiment	Depth at Fracture	Simulation Material Orientation	Effective Plastic Strain at Fracture
B1 and B2	20.75	0°	2.783
		45°	3.822
		90°	2.735
		Isotropic Curve	3.315
B3	20.50	0°	2.732
		45°	3.699
		90°	2.731
		Isotropic Curve	3.315

The results found in Table 23 show a maximum strain when the 45-degree orientation material is used. A similar trend as the one found with Wall Angle of UWA parts can be identified, where the values for the "Isotropic Curve" material behavior lie between the values obtained from 0 and 45 degrees. Once again this might suggest that a material model

that uses all three orientations at the same time, depending on direction the tool moves against the blank, might represent a solution like the “Isotropic Curve” results.

An effort should be made to measure the effective strain experimentally in order to verify the results obtained with the simulation.

Chapter Five: Conclusions and Outlook

The results found in the present work provide some useful insight into forming Stainless Steel AISI - 304 with Single Point Incremental Forming. An experimental formability limit was found with a maximum wall angle of 79.26°. For the design of parts, it is recommended to stay under 75° to stand clear of the found limit. Also, the sheet thinning according to the Cosine's law should be taken into account for future part design using this process.

Also, a clear effect of anisotropy was found on the effective plastic strain where 45° from rolling direction was found to have the greatest value. The effects of anisotropy on the wall thickness was also observed where again, at 45° from the rolling direction the results were significantly different. This coincides with the research done on Aluminum by Kumar *et al*. (2018), where the same direction was found to oppose deformation more than 0 and 90 degrees.

Finally, the effects of anisotropy on Wall Angle are not evident and seem non-significant.

This research opens a lot of doors for further investigation. Although Digital Image Correlation was attempted for the Tensile Tests, it was not successfully implemented. This technique needs to be successfully developed at UDLAP since the software and equipment necessary is available. This would provide further detail at the necking and strain concentration zone during a tensile test. This information could benefit the prediction of effective plastic strain using the FEM model greatly.

Also, further research could be done on the improvement of the FEM simulation model by means of experimenting with adaptive or sectionalized meshing to increase the accuracy. SPIF has very localized deformation so small element sizes is necessary, but a balance with computational cost needs to be found for the context of UDLAP. Additionally, the effects of springback should be modeled and simulated.

Furthermore, by having FEM material models for all three directions of anisotropy, a new model that uses all three models in the same simulation depending on the direction of deformation can be implemented. Inside the LS Pre-Post software the material configuration is called “Mat_3_Parameter_Barlat” and is the material 36. This line of research is already being worked on by the author of the present work.

On the grounds of formability, experimental measurements of variable wall angle parts should be conducted to obtain the major and minor strains around fracture points. This way a maximum major strain at zero minor strain (FLDo) can be defined and compared with the simulation results.

References

Ambrogio, G., De Napoli, L., FIlice, L., Gagliardi, F., & Muzzupappa, M. (2005). Application of Incremental Forming process for high customised medical product manufacturing. *Journal of Materials Processing Technology*, 156-162.

Belmont Galvez, A. (2018). *Comparison of two sheet metal forming processes: Conventional Stamping vs. Incremental Sheet Forming.* San Andres Cholula: Universidad de las Americas Puebla.

Centeno, G., Bagudanch, I., Martinez-Donaire, A., Gracia-Romeu, M., & Vallellano, C. (2014). Critical Analisys of Necking and Fracture Limit Strains and Forming Forces in Single-Point Incremental Forming. *Materials & Design*.

Fratini, L., Ambrogio, G., Di Lorenzo, R., Filice, L., & Micari, F. (2004). Influence of mechanical properties of the sheet material on formability in single point incremental forming. *CIRP Annals Manufacturing Technology*, 207-210.

Golabi, S., & Khazaali, H. (2014). Determining frustum depth of 304 stainless steel plates with various diameters and thicknesses by incremental forming. *Journal of Mechanical Science and Technology*, 3273-3278.

Gupta, P., & Jeswiet, J. (2017). Effect of temperatures during forming in single point incremental forming. *The International Journal of Advanced Manufacturing Technology*, 3693-3706.

Hirt, G., Ames, J., Bambach, M., & Kopp, R. (2004). Forming strategies and Process Modelling for CNC Incremental Sheet Forming. *Annals of CIRP*, 203.

Hussain, G., & Gao, L. (2007). A Novel method to Test the Thinning Limits of Sheet Metals in Negative Incremental Forming. *International Journal of Machine Tools & Manufacture*, 419-435.

Hussain, G., Gao, L., Hayat, N., & Ziran, X. (2008). A New Formability Indicator in Single Point Incremental Forming. *Journal of Materials Processing Technology*, 1-6.

Jeswiet, J., & Micari, F. (2005). Asymmetric Single Point Incremental Forming of Sheet Metal. *CIRP Annals - Manufacturing Technology*, 88-114.

Kumar Barnwal, V., Chakrabarty, S., Tewari, A., Narasimhan, K., & Mishra, S. K. (2018). Forming Behavior and microstructural evolution during single point incremental forming process of AA-6061 aluminum alloy sheet. *International Journal of Advanced Manufacturing Technology*, 921-935.

MatWeb, LCC. (2018). *matweb.com*. Retrieved from http://www.matweb.com/search/DataSheet.aspx?MatGUID=4b43bf1211e84673bae1b2b81c7a2c01

McAnulty, T., Jeswiet, J., & Doolan, M. (2016). Formability in single point incremental forming: A comparative analysis of the state of the art. *CIRP Journal of Manufacturing Science and Technology*, 1-12.

Perez Santiago, R. (2012). *Forming Force Estimation in Single Point Incremental Forming of Uniform and Variable Wall Angle Components.* Monterrey, N.L.: ITESM.

Shamsari, M., Mirnia, M. J., Elyasi, M., & Baseri, H. (2017). Formability improvement in single point incremental forming of truncated cone using a two-stage hybrid deformation strategy. *International Journal of Advanced Manufacturing Technology*, 2357-2368.

Wang, Y. H., Jiang, J., Wanintrudal, C. D., Zhou, D., Smith, L. M., & Yang, L. X. (2010). Field Sheet-Metal Tensile Test Using DIgital Image Correlation. *Experimental Techniques*, 54-59.

Wei, H., Gao, L., & Li, S. (2004). Investigation on thickness distribution along bulge type incrementally formed sheet metal part with irregular shapes. *Proceedings of the International Manufacturing Conference*, (pp. 1672-3961). Jinan.

Appendix A: Additional Figures

Specimen 2

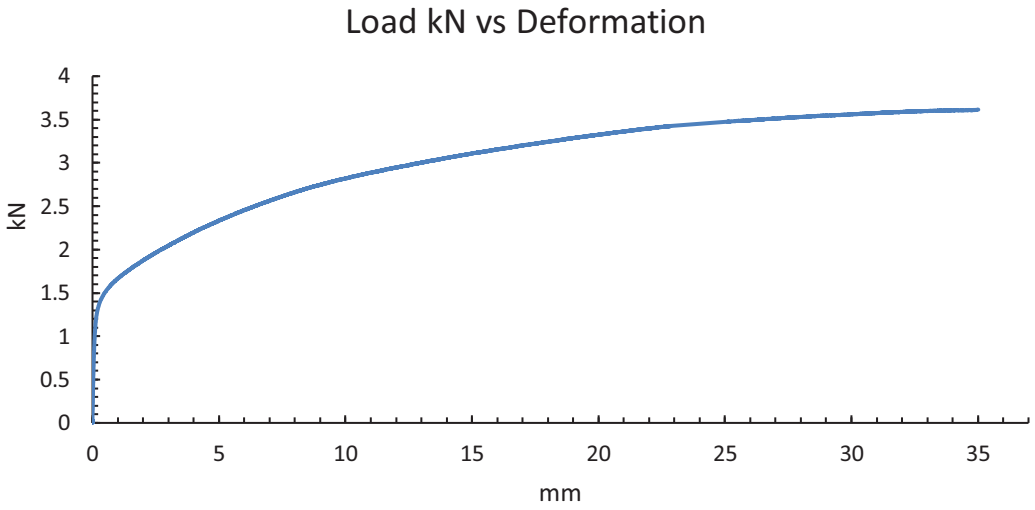

Figure 65. Load vs Deformation of Specimen 2

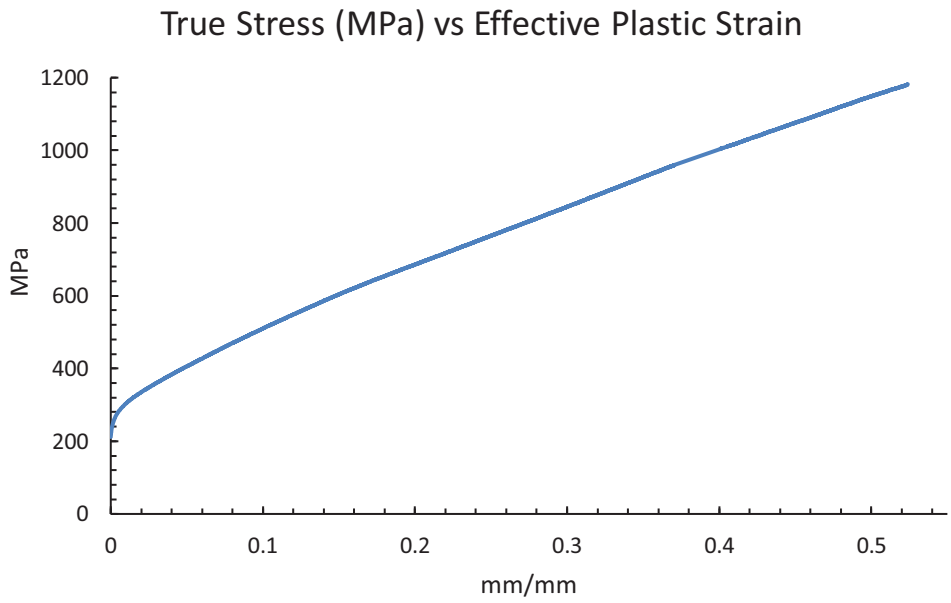

Figure 66. True Stress vs Effective Plastic Strain of Specimen 2

Specimen 4

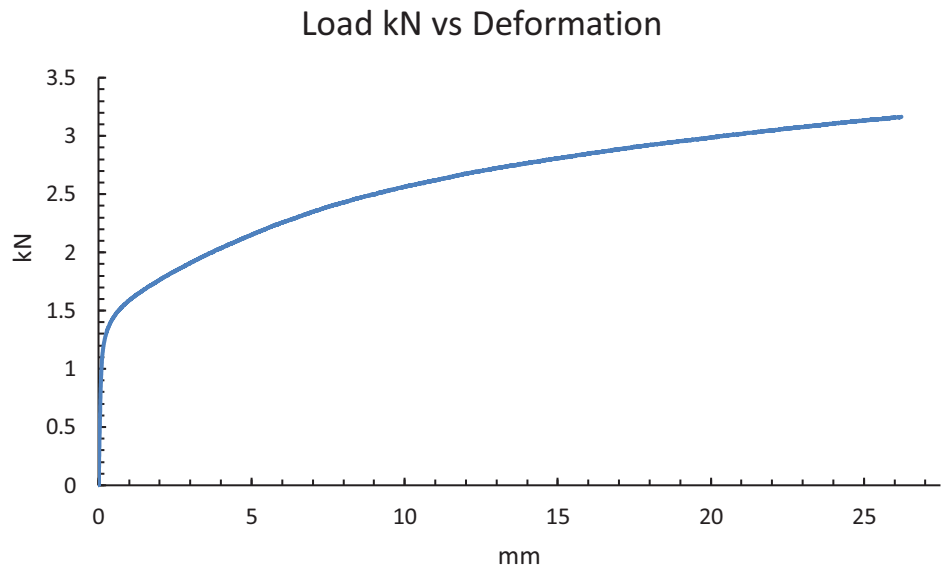

Figure 67. Load vs Deformation of Specimen 4

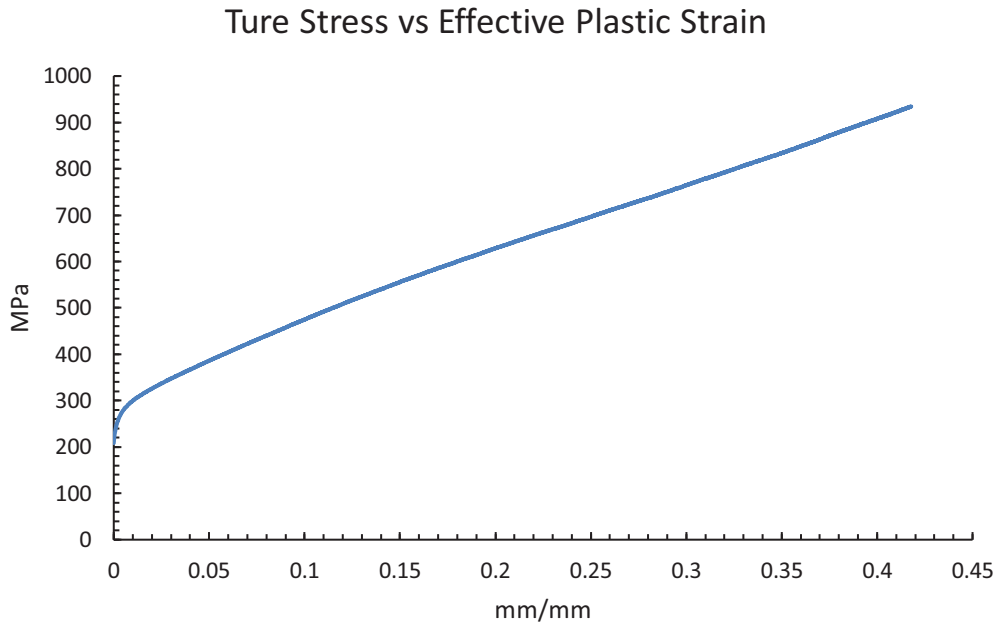

Figure 68. True Stress vs Effective Plastic Strain of Specimen 4

Specimen 5

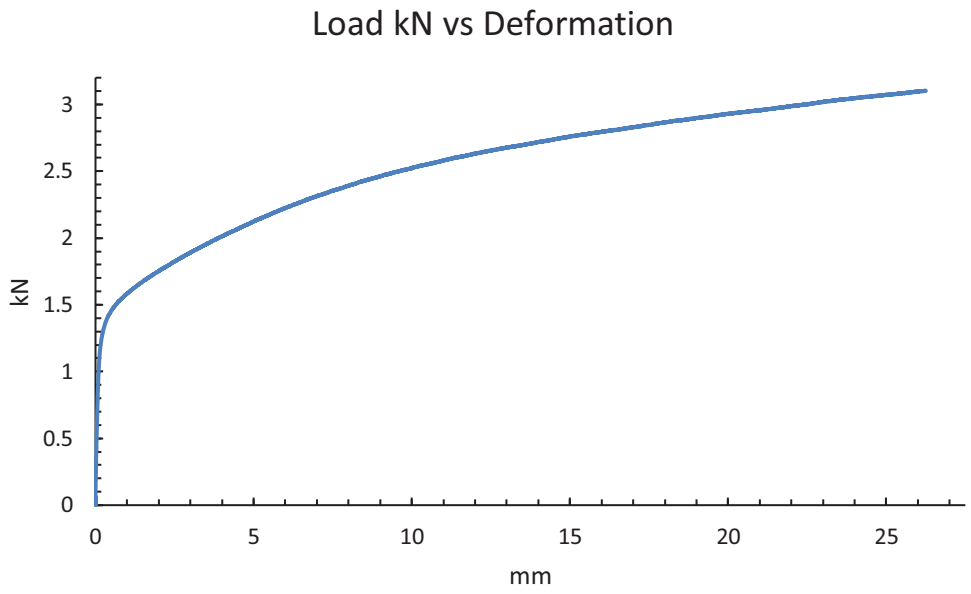

Figure 69. Load vs Deformation of Specimen 5

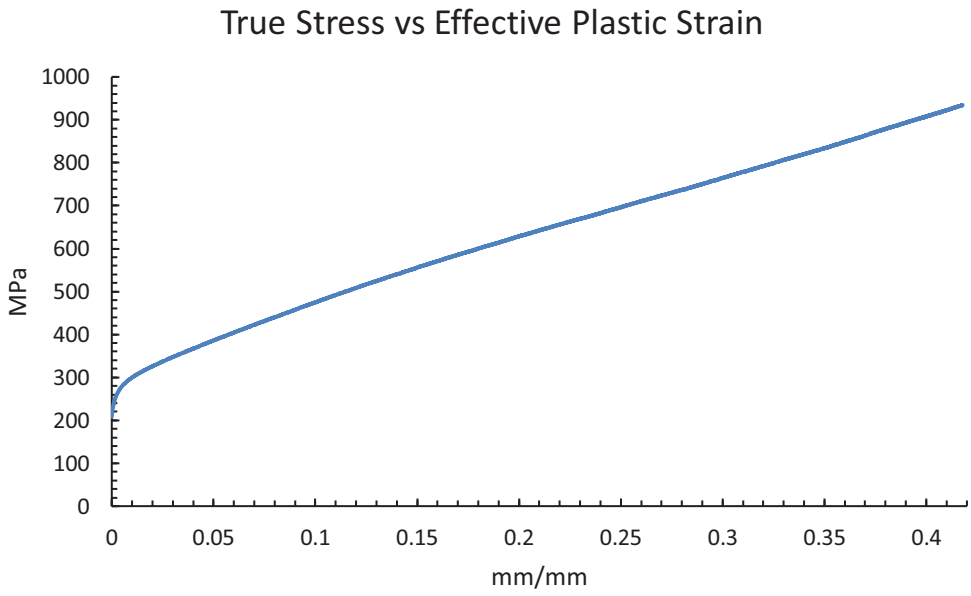

Figure 70. True Stress vs Effective Plastic Strain of Specimen 5

Specimen 8

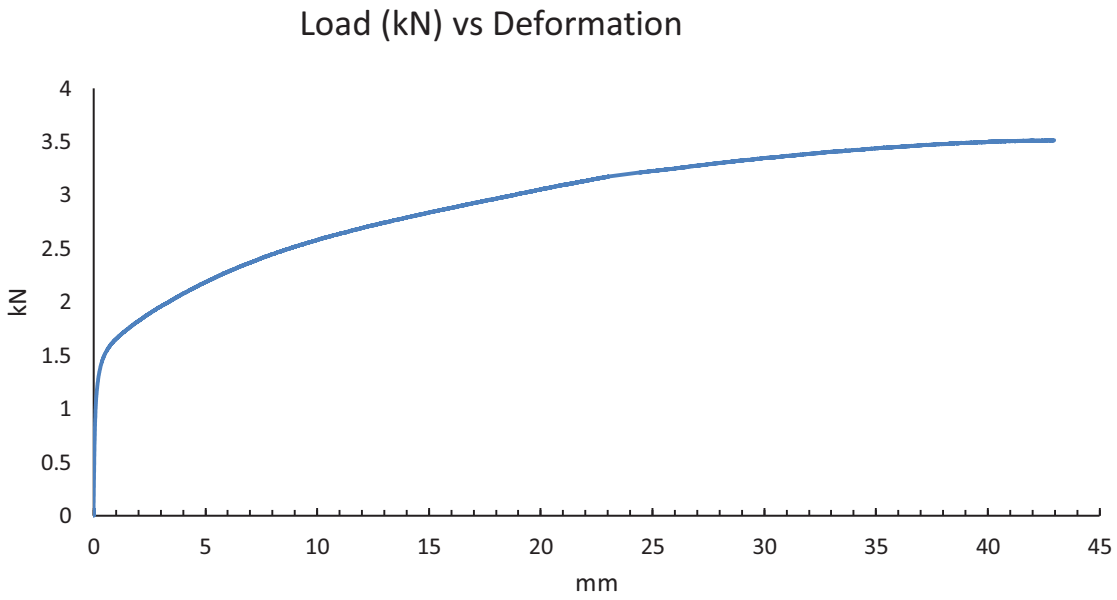

Figure 71. Load vs Deformation of Specimen 8

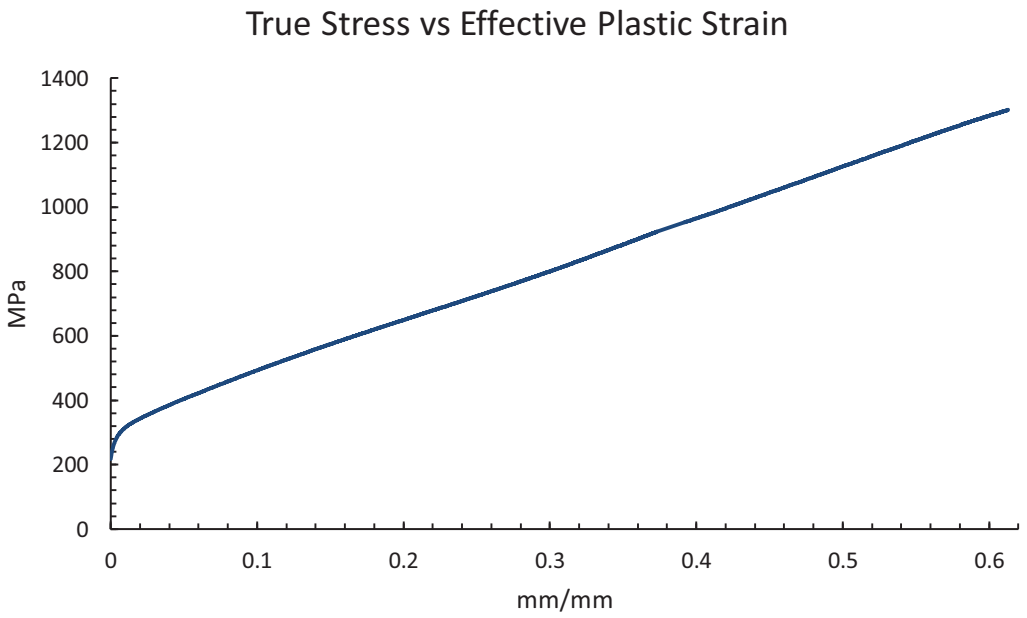

Figure 72. True Stress vs Effective Plastic Strain of Specimen 8

Appendix B: Technical Specifications of the Utilized Equipment

Table 24 Specifications of EMCO 500 Concept mill

Work Area	
Travel in X/Y/Z	190/140/260 mm
Distance spindle nose	77-337 mm
Number of axes	3rd (4th optionally)
Rapid motion	2 m/min
Feed force in X/Y/Z	800/800/1000 N
Clamping Area	420 x 125 mm
Max. table load	10 kg
Milling spindle	
Tool holder	EMCO similar SK30
Number of tools	8
Max. speed	3500 rpm
Max. Drive Power	0.75 kW
Max Torque	3.7 Nm

Table 25 Main Parameters of Universal Testing Machine WDW-300E

Main Parameters	
Max load capacity	300kN
Accuracy of the load	+- 0.5%
Measuring range of test load	.4% - 100%
Resolution of load	.001 %FN
Deformation measuring range	.2%- 100%
Deformation measuring accuracy	+-0.5%
Resolution displacement	.001 mm
Measuring accuracy of displacement	+- 0.5%
Speed range	0.005mm/min -500 mm/min
Accuracy of speed	+- 0.5%
Max tensile travel	600 mm
Max compression travel	600 mm
Width for testing space	760 mm
Overall dimension	1870x770x2558 mm
Power supply	7.5 kW AC 380V
Weight	1660 Kg

Appendix C: Python Sub-Routines

Modified programs from the routines developed by Dr. Rogelio Perez Santiago

```
# zirl0lmpfpro.py
# Generador de puntos para formar cono/piramide(redondeada) truncados generatriz circular
# Los parametros de entrada son el numero de ciclos de la herramienta
# diametro externo del cono en mm(corregir en futuras versiones)
# los angulos inicial y final de formado en grados
# el paso vertical, en mm, deseado (cambiar a altura de cresta "scallop")
# Para utilizarlo, una vez configurado el "path" de python, 1)abrir
# una ventana DOS 2)teclear python zir3.py, 3) dar un nombre al archivo
# Ver c
# Se puede seleccionar entre rotacion en un sentido o alternado
# RPS, 15/02/11
# produce un codigo G en formato mpf
# contiene un contador "ernesto" que detiene el proceso cada 5mm para agregar lubricante
from __future__ import print_function
import os.path
import sys
import math
filenaml = 'pathxyz.dat'
filenam2 = 'pathxyz.mpf'
filenam3 = 'angles.txt'
filenam4 = 'xsection2.txt'

f=open(filenaml,'w')
f2=open(filenam2,'w')
f3=open(filenam3,'w')
f4=open(filenam4,'w')
#print(filename,file=f2)

#parameters (tres primeros son variables para ICTP)

Angulo=45.0      #EE
Radio_gen=40    #EE                          #0 for UWA and >0 for VWA
Diam_mayor=70  #EE

thetdl=Angulo                                #initial forming angle
thetrl=thetdl*math.pi/180
thetd2=80.0
thetr2=thetd2*math.pi/180
radl=Diam_mayor/2                            # long radius
rad2=Radio_gen                               # generatrix radius
hgth=rad2*math.cos(thetrl)                   #total heigth of cone

hgth=rad2*math.cos(thetrl)                  #total heigth of cone
delz=0.25                                   #delta z
dela=1.5*delz                               #curve arc length relative to delz (1.5 times delz)
#dlth=40                                    #initial forming angle
ipdv=60                                     #initial divisions for the in-plane radius (360 degrees base)
ipdv2=4                                     #initial divisions for the corner (90 degrees base)
cfact=0.2                                   #corner factor = corner radius/half side
trad=3.175              #EE                 #tool RADIUS not diameter
seczl=40.0                                  #security height 1
secz2=1.0                                   #security height 2
Nini=5                                      #initial index
wfed=500                                    #working feed (mm/min)
spis=1250                                   #spindle speed (rev/min)
srot=1                                      #sentido de rotacion, -1= constante, 1 = alternado
pira=1                                      #pyramidal =1, conical =0
numpasos=100                                 #cantidad de pasos
lfed=500                                    #feed after lubrication to aproach sheet
dec=0                                       #dec=1 time between lubrications decreases each time, dec=0 no ch
mod=0                                       #mayor mod= mayour decremento en tiempo entre lubricaciones
```

```
mod=0                                          #mayor mod= mayour decremento en tiempo entre lubricaciones
spis1=1250                                      #tiene cuatro diferentes spindle speeds y work feeds, el spis4 (
spis2=1250                                     #estos parámetros son para cada lado de la pirámide, el lado cuat
spis3=1250                                     #el lado 1 es el horizontal inferior, el lado 2 es el vertical de
spis4=1250                                     # y el lado 3 es el lado horizontal superior
wfed1=500
wfed2=500
wfed3=500
wfed4=500

if rad2==0:
        ncyc=numpasos
else:
        zthet2=hgth-rad2*math.cos(thetr2)
        ncyc=int(zthet2/delz)

dthdl=thetdl
#dell=delz/math.tan(dthr)                      #delta x-y
coran=math.acos((trad-delz)/trad)              #tool correction angle

x=y=z=dell=dlzt=0                              #!Zero in the center of the plate
srot1=1
delx=x+radl-trad*math.sin(coran)
```

```
print('N{0:} G90'.format(Nini),file=f2)
#Nind=Nini+5
#print('N{0:} S{1:} M3'.format(Nind,spis),file=f2)
Nind=Nini+5
print('N{0:} G507'.format(Nind),file=f2)
Nind=Nind+5
print('           X            Y            Z       angulo',file=f)
print('           Z       angulo',file=f3)
print('           X            Z       angulo',file=f4)
print('{0:12.7F} {1:12.7F} {2:12.7F} {3:12.7F}'.format(x,y,z,dthdl),file=f)
print('N{0:} G0X{1:7.3F} Y{2:7.3F} Z{3:7.3F}'.format(Nind,x,y,secz1),file=f2)
Nind=Nind+5
print('N{0:} G0X{1:7.3F} Y{2:7.3F} Z{3:7.3F}'.format(Nind,x,y,secz2),file=f2)
Nind=Nind+5
print('N{0:} G1 F{1:} X{2:7.3F} Y{3:7.3F} Z{4:7.3F}'.format(Nind,wfed,x,y,z),file=f2)      #wfed
ernesto=1
raz=20
if dec==0:
        mod=0

for i in range (0,ncyc+1):
        if srot==-1:
                srot1=-1*srot
                Nind=Nind+5
                print('N{0:} M5'.format(Nind),file=f2)
                Nind=Nind+5
                print('N{0:} S{1:} M4'.format(Nind,spis),file=f2)                          #spis
        elif srot==1:
                srot1=-1*srot1
                if srot1==-1:
                        Nind=Nind+5
                        if ernesto%raz==0:
                                print('N{0:} G0 Z40'.format(Nind),file=f2)
                                Nind=Nind+5
                                print('N{0:} M00'.format(Nind),file=f2)
                                Nind=Nind+5
                                print('N{0:} F{1:}'.format(Nind,lfed),file=f2)        #lfed
                                Nind=Nind+5
                                raz=raz-mod
                        print('N{0:} M5'.format(Nind),file=f2)
                        Nind=Nind+5
```

```
                Nind=Nind+5
                print('N{0:} S{1:} M4'.format(Nind,spis),file=f2)       #spis
        elif srot1==1:
                Nind=Nind+5
                if ernesto%raz==0:
                        print('N{0:} G0 Z40'.format(Nind),file=f2)
                        Nind=Nind+5
                        print('N{0:} M00'.format(Nind),file=f2)
                        Nind=Nind+5
                        print('N{0:} F{1:}'.format(Nind,lfed),file=f2)      #lfed
                        Nind=Nind+5
                        raz=raz-mod
                print('N{0:} M5'.format(Nind),file=f2)
                Nind=Nind+5

                print('N{0:} S{1:} M3'.format(Nind,spis),file=f2)            #spis

delx=delx-dell
delxnew=delx*cfact
print('{0:12.7F} {1:12.7F} {2:12.7F} {3:12.7F}'.format(delx,y,z-i*delz,dthdl),file=f)                          #deltax
print('{0:12.7F} {1:12.7F} {2:12.7F}'.format(delx,z-i*delz,dthdl),file=f4)
Nind=Nind+5
print('N{0:} G1X{1:7.3F} Y{2:7.3F} Z{3:7.3F}'.format(Nind,delx,y,z-i*delz),file=f2)
Nind=Nind+5
print('N{0:} F{1:}'.format(Nind,wfed),file=f2)                                          #wfed
print('{0:12.7F} {1:12.7F} {2:12.7F} {3:12.7F}'.format(delx,y,z-(i+1)*delz,dthdl),file=f)                      #indentation
Nind=Nind+5
ernesto=ernesto+1
"""if ernesto%20==0:
        #print('N{0:} G1X{1:7.3F} Y{2:7.3F} Zb{3:7.3F} Ernesto{4:7.3F}'.format(Nind,delx,y,z-(i+1)*delz,ernesto),file=f2)"""
print('N{0:} G1X{1:7.3F} Y{2:7.3F} Z{3:7.3F}'.format(Nind,delx,y,z-(i+1)*delz),file=f2)          #magia aqui
Nind=Nind+5
"""if ernesto%20==0:
        #print('N{0:} M00'.format(Nind),file=f2)
        #print('N{0:} G1X{1:7.3F} Y{2:7.3F} Zb{3:7.3F} Ernesto{4:7.3F}'.format(Nind,delx,y,z-(i+1)*delz,ernesto),file=f2)"""
if pira==0:
        radp=math.sqrt(math.pow(delx,2)+math.pow(y,2))
        perm=2*math.pi*radp
        ipdv=int(perm/dela)
        #ipdv=5
        dthr2=2*math.pi/ipdv                                                                                    #in pl
```

```
        dthr2=2*math.pi/ipdv                                                                    #in plane delta angle
        for j in range (1,ipdv+1):
                ipdlc=(delx)*math.cos(j*dthr2)                  #in plane delta cosine
                ipdls=srot1*(delx)*math.sin(j*dthr2)            #in plane delta sine
                print('{0:12.7F} {1:12.7F} {2:12.7F} {3:12.7F}'.format(ipdlc,ipdls,z-(i+1)*delz,dthdl),file=f)          #deltax, deltay
                Nindj=Nind+5*j
                print('N{0:} G1X{1:7.3F} Y{2:7.3F}'.format(Nindj,ipdlc,ipdls),file=f2)
else:
        #dell=delz/math.tan(athr) #delta x-y
        print('{0:12.7F} {1:12.7F} {2:12.7F} {3:12.7F}'.format(delx,(1-cfact)*delx*srot1,z-(i+1)*delz,dthdl),file=f)
        Nindj=Nind+5
        print('N{0:} G1X{1:7.3F} Y{2:7.3F}'.format(Nindj,delx,(1-cfact)*delx*srot1),file=f2)
        print(';lado1',file=f2)              #lado1
        Nindj=Nind+5
        print('N{0:} S{1:} F{2:}'.format(Nind,spis1,wfed1),file=f2)
        dthr2=2*math.pi/(4*ipdv2)
        for j in range (1,ipdv2+1):
                ipdlc=delxnew*math.cos(j*dthr2)                 #in plane delta cosine
                ipdls=srot1*delxnew*math.sin(j*dthr2)                   #in plane delta sine
                ipdlcn=srot1*delxnew*math.cos(j*dthr2)                  #in plane delta cosine
                ipdlsn=delxnew*math.sin(j*dthr2)                        #in plane delta sine
                print('{0:12.7F} {1:12.7F} {2:12.7F} {3:12.7F}'.format((1-cfact)*delx+ipdlc,(1-cfact)*delx*srot1+ipdls,z-(i+1)*delz,dthdl),file=f)
                Nindj=Nind+5*j
                print('N{0:} G1X{1:7.3F} Y{2:7.3F}'.format(Nindj,(1-cfact)*delx+ipdlc,(1-cfact)*delx*srot1+ipdls),file=f2)
        print('{0:12.7F} {1:12.7F} {2:12.7F} {3:12.7F}'.format(-(1-cfact)*delx,delx*srot1,z-(i+1)*delz,dthdl),file=f)
        Nindj=Nindj+5
        print('N{0:} G1X{1:7.3F} Y{2:7.3F}'.format(Nindj,-(1-cfact)*delx,delx*srot1),file=f2)
        print(';lado2',file=f2)                                 #lado 2
        Nindj=Nind+5
        print('N{0:} S{1:} F{2:}'.format(Nind,spis2,wfed2),file=f2)
        for j in range (1,ipdv2+1):
                ipdlc=delxnew*math.cos(j*dthr2)                 #in plane delta cosine
                ipdls=srot1*delxnew*math.sin(j*dthr2)                   #in plane delta sine
                ipdlcn=srot1*delxnew*math.cos(j*dthr2)                  #in plane delta cosine
                ipdlsn=delxnew*math.sin(j*dthr2)                        #in plane delta sine
                print('{0:12.7F} {1:12.7F} {2:12.7F} {3:12.7F}'.format(-(1-cfact)*delx-ipdlsn,(1-cfact)*delx*srot1+ipdlcn,z-(i+1)*delz,dthdl),file=f)
                Nindj=Nind+5*j
                print('N{0:} G1X{1:7.3F} Y{2:7.3F}'.format(Nindj,-(1-cfact)*delx-ipdlsn,(1-cfact)*delx*srot1+ipdlcn),file=f2)
        print('{0:12.7F} {1:12.7F} {2:12.7F} {3:12.7F}'.format(-delx,-(1-cfact)*delx*srot1,z-(i+1)*delz,dthdl),file=f)
        Nindj=Nindj+5
        print('N{0:} G1X{1:7.3F} Y{2:7.3F}'.format(Nindj,-delx,-(1-cfact)*delx*srot1),file=f2)
```

```
            print('(0:12.7F) (1:12.7F) (2:12.7F) (3:12.7F)'.format(-delx,-(1-cfact)*delx*srot1,z-(i+1)*delz,dthdl),file=f)
            Nindj=Nindj+5
            print('N(0:) G1X(1:7.3F) Y(2:7.3F)'.format(Nindj,-delx,-(1-cfact)*delx*srot1),file=f2)
            print(':ladc3',file=f2)                          #ladc3
            Nindj=Nind+5
            print('N(0:) S(1:) F(2:)'.format(Nind,spis3,wfed3),file=f2)
            for j in range (1,ipdv2+1):
                    ipdlc=delxnew*math.cos(j*dthr2)                 #in plane delta cosine
                    ipdls=srot1*delxnew*math.sin(j*dthr2)                   #in plane delta sine
                    ipdlcn=srot1*delxnew*math.cos(j*dthr2)                  #in plane delta cosine
                    ipdlsn=delxnew*math.sin(j*dthr2)                        #in plane delta sine
                    print('N(0:) (1:12.7F) (2:12.7F) (3:12.7F)'.format(-(1-cfact)*delx-ipdlc,-(1-cfact)*delx*srot1-ipdls,z-(i+1)*delz,dthdl),file=f)
                    Nindj=Nind+5*j
                    print('N(0:) G1X(1:7.3F) Y(2:7.3F)'.format(Nindj,-(1-cfact)*delx-ipdlc,-(1-cfact)*delx*srot1-ipdls),file=f2)
            print('(0:12.7F) (1:12.7F) (2:12.7F) (3:12.7F)'.format((1-cfact)*delx,-delx*srot1,z-(i+1)*delz,dthdl),file=f)
            Nindj=Nindj+5
            print('N(0:) G1X(1:7.3F) Y(2:7.3F)'.format(Nindj,(1-cfact)*delx,-delx*srot1),file=f2)
            print(':ladc4',file=f2)                  #ladc4
            Nindj=Nind+5
            print('N(0:) S(1:) F(2:)'.format(Nind,spis4,wfed4),file=f2)
            for j in range (1,ipdv2+1):
                    ipdlc=delxnew*math.cos(j*dthr2)                 #in plane delta cosine
                    ipdls=srot1*delxnew*math.sin(j*dthr2)                   #in plane delta sine
                    ipdlcn=srot1*delxnew*math.cos(j*dthr2)                  #in plane delta cosine
                    ipdlsn=delxnew*math.sin(j*dthr2)                        #in plane delta sine
                    print('(0:12.7F) (1:12.7F) (2:12.7F) (3:12.7F)'.format((1-cfact)*delx+ipdlsn,-(1-cfact)*delx*srot1-ipdlcn,z-(i+1)*delz,dthdl),file=f)
                    Nindj=Nind+5*j
                    print('N(0:) G1X(1:7.3F) Y(2:7.3F)'.format(Nindj,(1-cfact)*delx+ipdlsn,-(1-cfact)*delx*srot1-ipdlcn),file=f2)
            print('(0:12.7F) (1:12.7F) (2:12.7F) (3:12.7F)'.format(delx,y,z-(i+1)*delz,dthdl),file=f)
            Nindj=Nindj+5
            print('N(0:) G1X(1:7.3F) Y(2:7.3F)'.format(Nindj,delx,y),file=f2)


    lhth=hgth+dlzt
    if radl==0:
            dthr=thetrl
    else:
            dthr=math.acos(lhth/radl)

    dthdl=(dthr*180)/math.pi



        dthdl=(dthr*180)/math.pi
        print('(0:12.7F) (1:12.7F)'.format(z-i*delz,dthdl),file=f3)
        dell=(delz)/math.tan(dthr)
        dlzt=dlzt-delz
        Nind=Nindj

Nind=Nind+5
print('N(0:) G0X(1:7.3F) Y(2:7.3F) Z(3:7.3F)'.format(Nind,0,0,seczl),file=f2)
Nind=Nind+5
print('N(0:) M30'.format(Nind),file=f2)

f.close
f2.close
f3.close
f4.close
```

Second subroutine verliz5b.py:

```
#program to generate trapezoidal velocity curves
from __future__ import print_function
import os.path
import sys
import math

#filename = raw_input('Filename?\n')
filename='pathxyz.dat'

xl=yl=zl=0
t0=0

#parameters
rfeed=0.033                             #physical feed in m/s
mxtvl=2.0                               #initial max tool feed in mm/ms
rtime=2.0                               #rise time
ftime=100                               #physical rise time in ms
mxtv=mxtvl                              #max tool feed in mm/ms

fl=open(filename,'r')
f2=open('velxn.k','w')
f3=open('velyn.k','w')
f4=open('velzn.k','w')
f5=open('data.dat','w')
print(filename,file=f5)

linx=liny=linz=1                #only to count lines
inpl=timetot=timefis=0

#print('{0:11.5F} {1:11.5F}'.format(xl,t0),file=f2)
#print('{0:11.5F} {1:11.5F}'.format(yl,t0),file=f3)
#print('{0:11.5F} {1:11.5F}'.format(zl,t0),file=f4)
lvelx=[]
lvely=[]
lvelz=[]
ltime=[]

pathinput=fl.readlines()
for line in pathinput[2:]:
        info=line
        #info2=f6.readline()
```

```
pathinput=f1.readlines()
for line in pathinput[2:]:
        info=line
        #info2=f6.readline()
        inpl=inpl+1
        x2=info[0:12]
        y2=info[13:25]
        z2=info[26:38]
        a2=info[39:51]
        angulo=float(a2)
        delx=float(x2)-x1
        dely=float(y2)-y1
        delz=float(z2)-z1
        #print(delx,file=f2)
        #print(dely,file=f3)
        #print(delz,file=f4)
        deldis=math.sqrt(delx*delx+dely*dely+delz*delz)
        if deldis==0:
                continue
        elif deldis<4.1:
                mxtv=deldis/3.0
        else:
                mxtv=mxtv1
        dtim=(deldis-mxtv*rtime)/mxtv+2*rtime
        dtimf=(deldis-rfeed*ftime)/rfeed+2*ftime
        timetot=timetot+dtim
        timefis=timefis+dtimf
        if dtim==4:
                print('{0:11.5F} {1:11.5F} {2:} {3:}'.format(delx,dely,inpl,info),file=f5)


        else:
                print('{0:11.5F} {1:11.5F} {2:11.5F} {3:11.5F} {4:} {5:}'.format(deldis,timetot,timefis,angulo,inpl,linx),file=f5)
                ltime.append(t0+rtime)
                lvelx.append(mxtv*delx/deldis)
                ltime.append(t0+dtim-rtime)
                lvelx.append(mxtv*delx/deldis)
                ltime.append(t0+dtim)
                lvelx.append(0)
                linx=linx+3
                lvely.append(mxtv*dely/deldis)
                lvely.append(mxtv*dely/deldis)
                lvely.append(0)
                liny=liny+3
                lvelz.append(mxtv*delz/deldis)
                lvelz.append(mxtv*delz/deldis)
                lvelz.append(0)
                linz=linz+3
                t0=t0+dtim
                x1=float(x2)
                y1=float(y2)
                z1=float(z2)

print('*KEYWORD',file=f2)
print('*DEFINE_CURVE_TITLE',file=f2)
print('X VEL',file=f2)
print('         1         0  1.000000  1.000000',file=f2)
print('{},{}'.format(0,0),file=f2)
for num in range (0,linx-1):
        print('{},{}'.format(ltime[num],lvelx[num]),file=f2)
print('*END',file=f2)
print('{},{}'.format(ltime[num],lvelx[num]),file=f2)

print('*KEYWORD',file=f3)
print('*DEFINE_CURVE_TITLE',file=f3)
print('Y VEL',file=f3)
print('         2         0  1.000000  1.000000',file=f3)
print('{},{}'.format(0,0),file=f3)
for num in range (0,linx-1):
        print('{},{}'.format(ltime[num],lvely[num]),file=f3)
print('*END',file=f3)



# info=f.readline()
f1.close
f2.close
f3.close
f4.close
f5.close
```